Carbon Capture Science & Technology 5 (2022) 100079

Contents lists available at ScienceDirect

Carbon Capture Science & Technology

journal homepage: www.elsevier.com/locate/ccst

Full Length Article

Well-based monitoring of CO_2 geological sequestration operations in saline aquifers: Critical insights into key questions

Y. Zapata[a], M.R. Kristensen[b], N. Huerta[c], C. Brown[c], C.S. Kabir[d,*], Z. Reza[a]

[a] University of Oklahoma, Norman, OK, USA
[b] Schlumberger, Cambridge, MA, USA
[c] Pacific Northwest National Laboratory, Richland, WA, USA
[d] Incendium Technologies, Round Rock, TX, USA

ARTICLE INFO

Keywords:
CO_2 injection
Solubility trapping
Plume dynamics
Salinity & density
pH change
Carbon storage

ABSTRACT

Geological carbon sequestration in saline aquifers is one of the most promising strategies to help mitigate emissions of CO_2 to the atmosphere. Significant challenges in ensuring the security of the sequestration process rest in the evolution and expansion of the CO_2 plume in the subsurface. The ability to track the movement of the injected CO_2 poses another challenge. Critical questions related to the integrity of the sequestration operations in saline aquifers relate to plume characteristics that can we monitor using well-based variables. We addressed this and related questions using an integrated modeling framework through a numerical investigation of carbon sequestration in saline aquifers during long-term and post-injection periods. This modeling paradigm incorporates the effect of structural, geological, and petrophysical characteristics. That way, we can account for critical physicochemical processes, rock-fluid interactions, and lithology dependencies. The well fluid variables investigated include fluid composition, pH, fluid density, and ion activity. We learned that fluid property analytics and diagnostics can be powerful tools to estimate the movement of CO_2 and its storage in different trapping mechanisms. These analytics can help optimize operational aspects and simplify reservoir-scale models while still reflecting the complex nature of the CO_2 interactions underground and offering insights into plume evolution.

1. Introduction

Carbon sequestration in saline aquifers holds great potential in mitigating greenhouse gas emissions to the atmosphere. Successful implementation of CO_2 storage projects requires management strategies that track the displacement of the injected CO_2 in the subsurface within technical and economic limits. Numerical simulation and monitoring, verification, and accounting tools (MVA) are necessary to predict storage capacity and assess the long-term risk arising from fault activation or wellbore leakage. In other words, plume monitoring (CO_2-plume migration tracking), assurance monitoring (assessment of leakage risk), and validation of modeling tools are essential components of storage project management to improve the operational success of a carbon sequestration project. MVA activities associated with CO_2 sequestration differ from site characterization, including plume tracking, leak detection, caprock integrity, and long-term post-injection monitoring (Plasynski et al., 2011). Many physical, chemical, and biological parameters are measured based on techniques practiced in waste disposal, groundwater management, and oil and gas production (Benson et al., 2005; Gogri et al., 2018; Phan et al., 2018).

Although our focus is on subsurface carbon sequestration, some latest review articles paint optimistic pictures about other ways of retaining carbon. For example, Nayank et al. (2022) discussed biomass and enhanced soil carbon methods for carbon retention. Similarly, Buckingham et al. (2022) explored various solid CO_2 adsorbents. They observed that although alkali earth metal oxides and ceramics offer good promise, new adsorbents must be developed for higher thermal stability at intermediate to elevated temperatures. Carbon capture and storage, or CCS, presents many operational challenges. They include salt clogging during supercritical CO_2 injection (Berntsen et al., 2019; Miri and Hellevang, 2016; Norouzi et al., 2021), caprock integrity in chalk formations (Bonto et al., 2021), and thermal stress on wellbore integrity (Roy et al., 2018), among others.

Let us point out that CCS is active in the USA and other countries. In the US, as of November 2019, Beck (2020) reported that 10 CCS active facilities sequestered 25 Mt per annum. Globally, among the 27

Abbreviations: CCS, Carbon capture and storage; DoE, Design of Experiments; GMS, Gas membrane sensor; MVA, Monitoring, verification, and accounting; OBM, Object based modeling; SIS, Sequential indicator simulation; TDS, Total dissolved solids.

* Corresponding author at: Incendium Technologies, Inc., 1700 Bryant Dr. Suite 105, Round Rock, TX 78664, United States.
E-mail address: shah@incendiumtech.com (C.S. Kabir).

https://doi.org/10.1016/j.ccst.2022.100079
Received 18 August 2022; Received in revised form 3 November 2022; Accepted 4 November 2022

operating CCS facilities in 2021, about 36.6 Mt of CO_2 can be stored annually, as reported by Global CCS Institute (2021). Given that the global aim is to reach the net-zero CO_2 emission target by 2050, in-depth probing of the CCS technology becomes imperative. In this regard, two populous countries are taking specific steps as articulated in review articles by Shaw and Mukherjee (2022) and Bokka et al. (2022) for India, and Li et al. (2021) and Jiang et al., 2020 for China. Overall, Ringrose (2020) provides insights into CO_2 underground storage projects. To that end, Martin-Roberts et al. (2021), while providing a holistic picture of the status of CCS projects worldwide, showed that a gap exists between what was promised and delivered in actual field settings.

CO_2 monitoring techniques can be categorized into deep-focused and shallow-focused measurements. Shallow-focused tools enable monitoring to study CO_2 concentration in the atmosphere, ocean, or surface by directly measuring site leakage. Examples of shallow-focused techniques include sampling soil and surface gas flux, as shown in Beaubien et al. (2013), Fessenden et al. (2010), and Jones et al. (2011). In contrast, deep-focused techniques are used mainly for plume monitoring but can also apply to assurance monitoring (Hannis, 2013; Jenkins et al., 2015). These latest techniques involve geophysical monitoring, well-based monitoring, and geochemical monitoring.

Geophysical monitoring takes advantage of the high imaging potential of seismic techniques to detect changes caused by CO_2 in the compressional wave velocity and attenuation, facilitating fluid migration mapping. The most common tools are time-lapse seismic monitoring (4D seismic), vertical seismic profiling, and cross-well imaging (Chadwick et al., 2009; Hovorka et al., 2006; Karstens et al., 2017). On the other hand, well-based monitoring techniques include permanently deployed downhole sensors and specific time-lapse downhole surveys such as wireline logging (Freifeld et al., 2009; Würdemann et al., 2010; Xue et al., 2006). Permanent downhole sensors are critical for pressure and temperature monitoring, widely recognized as essential for maintaining operational integrity and leak detection (Park et al., 2013; Sun et al., 2016). This step is prevalent in oil and gas well operations. Specifically, Rocha-Valadez et al. (2014) demonstrated how analytical modeling could reveal the degree of leakage with the monitored annular-casing pressure data, both in production wells and in a CO_2-sequestered well. Gholami et al. (2021) also articulate a leak detection strategy.

Well-based monitoring can accompany geochemical tracking to evaluate the changes in fluid properties and account for the impact of these changes on the safe storage of CO_2 in saline aquifers. Collecting fluid samples from observation wells is the most common approach to investigate variations in brine and gas composition, the presence of tracers, and pH measurements (Benson and Cole, 2008; Freifeld et al., 2009; Hannis, 2013; Roberts et al., 2017). Of these, pH is the most important diagnostic indicator of the brine-CO_2 interaction. Specific downhole fluid geochemical methods have been developed to assess CO_2 storage sites, including the gas membrane sensor (GMS) and the U-tube fluid sampling system used, for example, at Ketzin and the Frio pilot sites (Freifeld et al., 2005; Martens et al., 2015). The GMS separates the gases dissolved in the fluid and pushes them to the surface to measure dissolved CO_2 concentrations downhole. The U-Tube system allows the operator to bring a sample to the surface while maintaining subsurface conditions, thereby avoiding degassing, among others, and then measures these parameters at the surface but under pressure. These parameters include density, pH, alkalinity, and gas composition.

One of the main areas of interest concerning the monitoring and simulation of CO_2 injection and storage in saline aquifers is understanding the CO_2-brine-rock interaction (Jayasekara et al., 2020). When massive amounts of CO_2 get injected underground, the chemical equilibrium of the system is disturbed. As a result, chemical reactions occur between the CO_2 and aquifer fluid and the fluid and the rock minerals. These reactions depend on the rock mineralogy, brine composition, aquifer temperature, and pressure. Moreover, these interactions are responsible for the changes in the aquifer fluid properties, such as pH and density, and the immobilization of the injected CO_2 via different trapping mechanisms, such as solubility and mineral trapping (Black et al., 2015; De Silva et al., 2015). Solubility trapping consists of the CO_2 retention in the aqueous phase as a function of the CO_2 solubility in the brine. Mineral trapping relates to the precipitation of carbonate minerals, such as calcite or dolomite, which can permanently immobilize the injected CO_2.

Several geochemical monitoring strategies have analyzed injection and post-injection fluid samples in the pilot and commercial CO_2 sequestration projects worldwide to determine the fluid chemistry and isotope composition changes. For instance, in the Weyburn field in Canada (Emberley et al., 2004), tracking pH, salinity, and isotopic data allowed investigation of the dissolution of carbonate minerals that promoted solubility trapping of CO_2 and provided estimates of the storing capacity of dissolved CO_2 per liter of brine. In addition to monitoring tools, changes in pressure and geochemical data, such as pH or total dissolved solids (TDS), based on synthetic data generated for aquifers of interest have been used as indicators of CO_2 and brine leakage to help define appropriate spatial and time scales for injection and post-injection operations (Trainor-Guitton et al., 2016). Furthermore, geochemical simulations of dissolution and precipitation reactions based on reactive transport models have been implemented to evaluate caprock integrity and assess mineral trapping (Amin et al., 2014; Xu et al., 2004).

The data obtained from monitoring and verification lend themselves to inputs and constraints for numerical modeling schemes to evaluate an injection site's behavior and performance. Based on the information collected, robust numerical approaches aim to facilitate subsurface risk assessment associated with commercial-scale carbon sequestration. This information includes seismic surveys, wireline logging, fluid samples, and other data combined with 3D representations of the aquifers that consider fundamental geological and petrophysical properties (Dai et al., 2014; Savioli et al., 2017; Vo Thanh et al., 2019). Besides risk assessment, another critical aspect of the models is the sensitivity and uncertainty characterization to incorporate uncertain parameters' impact and distributions on evaluating the site's capacity and CO_2 storage by various mechanisms. Relevant variables include geological spatial variability, petrophysical properties, multiphase displacement behavior, and geomechanical parameters. Also, operational constraints, as discussed by Cao et al. (2020); Deng et al. (2012); Lengler et al. (2010); Sarkarfarshi et al. (2014); and Zapata et al. (2020) become relevant.

In this study, we employed an integrated workflow to monitor the evolution of CO_2 in the supercritical and aqueous phases during a carbon sequestration operation in a saline aquifer. We framed our investigation metrics around selected geochemical parameters, including fluid composition, pH, fluid density, and effective concentration of carbonate species in the aqueous phase. Although downhole monitoring of pressure and temperature data and their analyses provide the efficacy of the injection process, we constrained our focus on learning the plume dynamics for brevity in this article. So, we confined our investigation to the plume characteristics and evolution by tracking variations in the fluid properties and accounting for the CO_2-brine-rock interaction. We followed a modular methodology in an integrated modeling framework. The modules include:

1. Static modeling that consists of the construction of 3D stratigraphic, lithological, and petrophysical models.
2. Dynamic simulation of CO_2 injection physicochemical processes, rock-fluid interactions, and lithology dependencies.
3. Sensitivity and uncertainty analysis to determine the relative influence of selected parameters on the CO_2 plume characteristics and the storage of CO_2 through different trapping mechanisms; and
4. Analyses of "monitorable" fluid properties and the studies of the CO_2 plume evolution for both near-wellbore and the overall plume regions.

The following section describes the integrated modeling framework and the experimental design considered in this investigation. A

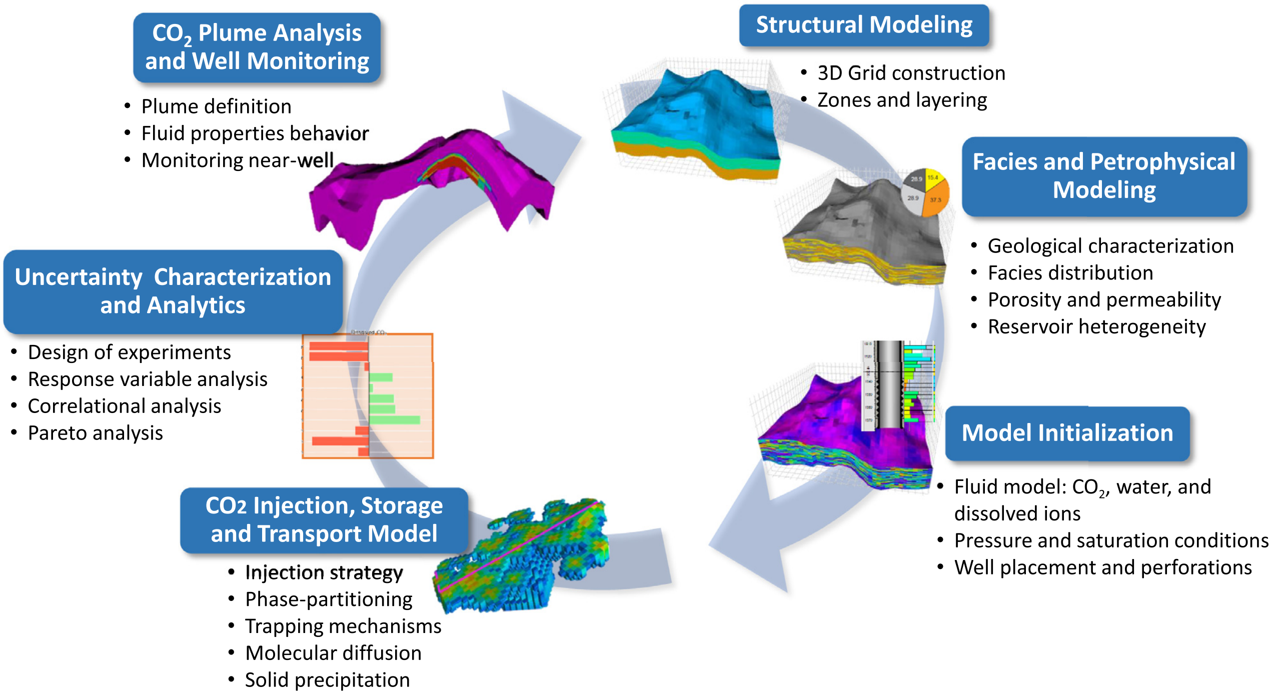

Fig. 1. CO_2 storage and transport model workflow helped study the evolution of CO_2 plume and aquifer properties during CO_2 injection into saline aquifers.

more detailed description of the methodologies employed appears in Zapata (2020) and Zapata et al. (2020). Subsequent sections will present discussions on the vital monitoring questions examined.

2. Modeling methodology

2.1. Integrated modeling framework

This study applied an integrated modeling framework to investigate well-based monitoring options for carbon sequestration in saline aquifers. The methodology has six main components. Integrated modeling typically starts with static modeling components. We constructed three-dimensional (3D) models to represent the aquifer formations by incorporating structural, lithological, and petrophysical properties. The next element is the parametrization of the fluids (brine and CO_2) and fluid-rock (CO_2-brine-rock) interactions accounting for changes in fluid composition, temperature, pressure, and other corresponding thermophysical properties. Subsequently, relevant transport physics, fluid phase equilibria, and trapping mechanisms governing the displacement and storage of CO_2 in the subsurface get incorporated. After all the modeling inputs, the numerical simulation of the reservoir dynamics starts with the model initialization and design of experiments.

Design of experiments (DoE) typically involves sensitivity and uncertainty characterization of the response variables of interest due to variability in static and dynamic modeling parameterization and uncertain variables. In other words, several scenarios helped assess the effects of various parameters on the simulation response variables, including geological, petrophysical, and injection variables. The last leg of the integrated methodology involves post-simulation analytics. Here, we investigate various well-based variables that one can monitor to decipher the spatial and temporal characteristics of the CO_2 plumes in saline aquifers. Fig. 1 shows a schematic representation of the workflow employed. A comprehensive description of the workflow development follows.

In this manuscript, for the integrated modeling workflow for CO_2 storage and transport in saline aquifers, we followed the schematic outlined in Zapata et al., 2020. In gist, for the structural framework of realistic subsurface geological formations, the 3D grid representing the saline aquifer's static geological models contains 75,200 grid cells (40 × 40 × 47 cells), with an areal extent of 3 km × 3 km and thickness varying from 120 to 280 m with an average of 203 m. The lateral dimensions for the grid cells in - and -directions are 75 m, and the average thickness is 4.4 m. The structure is divided into four zones, as shown in Fig. 2a. The storage formation is in Zone 4, the lowermost zone. Zone 1 acts as the caprock. Zone 2 represents another suitable layer for CO_2 injection, and Zone 3 serves as a flow baffle and barrier to separate the primary formation of the study. The layering of each zone is assigned to capture the heterogeneity of the local geological features at this scale, with 47 layers distributed as 2, 22, 1, and 22 layers in each zone, respectively.

After the structural framework, 3D models are developed using lithology (facies) and lithology-constrained petrophysical properties representing the aquifer formations. We generated 3D facies models accounting for three main facies that are commonly present in fluvial deposits in saline aquifers and adjacent formations, namely sand, shaly sand, and shale, using sequential indicator simulation (SIS) and object-based modeling (OBM), as discussed by Deutsch and Journel (1998). The SIS technique helped generate the facies conditional probability distribution for Zones 1, 2, and 3. In contrast, the OBM approach helped determine the facies distribution of Zone 4 and capture the central geological bodies, such as sandstone channels, that are characteristic of the depositional environment. We used conditional two-point geostatistical (sequential Gaussian simulation) for petrophysical properties, such as porosity and permeability (Deutsch and Journel, 1998). The base-case porosity model distribution ranges between 3 and 28 %, with an average of 9%, and the corresponding permeability model values are between 0.01 and 40 mD, with an average of 3.02 mD.

Next, we focused on the fluids and rock-fluid interaction characterization. A multicomponent fluid model using five components becomes the focal point of this study. These five components are H_2O, CO_2, $NaCl$, $CaCl_2$, and $CaCO_3$, co-existing in three phases. The supercritical or free-phase implies CO_2-rich (gas-like viscosities and liquid densities), an aqueous phase (H_2O-rich, with the presence of CO_2 and dissolved salts), and solid components (salts and calcite). The supercritical CO_2 and solid

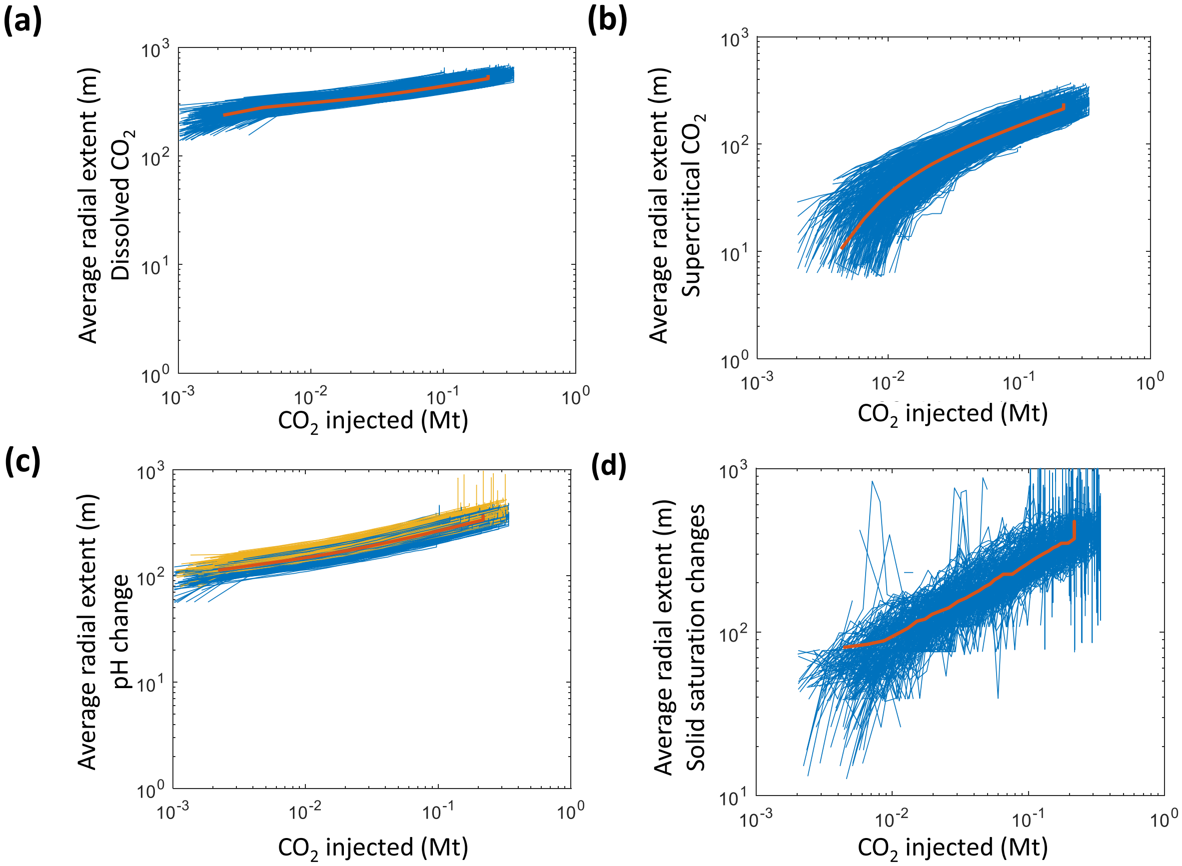

Fig. 2. CO_2 plume average radial extension with CO_2 injected for all case scenarios based on (a) CO_2 in the aqueous phase; (b) CO_2 in the supercritical phase; (c) pH change, the role of initial composition is highlighted for cases with initial calcite (blue) and without initial calcite (yellow); (d) changes in solid saturation related to dissolution. The blue lines represent the radial extension for individual cases, and the orange lines represent the average radial extension and CO_2 injection total among all cases studied.

components (NaCl, $CaCl_2$, and $CaCO_3$) interact with water and exist in the aqueous phase. For the CO_2-brine interaction, the chemical reactions within the aqueous phase modeled in our simulations include dissociating CO_2 into bicarbonate and carbonate ions (HCO_3^- and CO_3^{-2}). In comparison, the reactions between the solid components and the aqueous phase considered are the dissolution and precipitation of sodium chloride (NaCl), calcium chloride ($CaCl_2$), and calcite ($CaCO_2$).

For a detailed discussion of the study's thermophysical properties and fluid-phase equilibria models, refer to Zapata et al. (2020). We used the Spycher and Pruess (2005) model for the mutual solubilities to describe interactions of species between the supercritical CO_2 and the aqueous phase, based on the model formulated for a CO_2 – H_2O system. Their model considers corrected activity coefficients to include the effect of dissolved salts in the aqueous phase. Aqueous species in the brine play a role in CO_2 storage by affecting the CO_2 solubility and favoring or hindering reactions with the rock resulting in the precipitation or dissolution of additional minerals. The solubility of CO_2 in brine is a function of pressure, temperature, salinity, and brine composition. CO_2 solubility decreases with increasing temperature and salinity and increases with increasing pressure (Duan and Sun, 2003). The aqueous phase density modeling (including H_2O, CO_2, and salts) followed the modified-Ezrokhi's method to include the effect of dissolved CO_2 and salts (Zaytsev and Aseyev, 1992). The density is determined for the CO_2 in the supercritical phase based on the modified-Redlich-Kwong equation-of-state, including a modified attraction parameter for temperature dependency (Spycher, Pruess, and Ennis-King, 2003). The viscosity was calculated as a function of temperature and density using the Vesovic et al. (1990) and Fenghour et al. (1998) methods.

An essential aspect of CO_2 dynamics involves the relevant transport physics considered. Besides advection and buoyancy-driven flow, molecular diffusion of CO_2 and other ions present in the fluid plays a vital role in the transport of CO_2 in the subsurface, given that diffusive processes can have an impact on the reaction rates between CO_2 and other components at the pore level (Steefel, 2008). It is necessary to determine the diffusion coefficients of the system components in aqueous and supercritical (CO_2) phases to characterize the CO_2 transport due to component concentration gradients. The diffusion coefficients implemented in this study account for the diffusion of water and CO_2 in both phases. We calculated the diffusion coefficients for water and CO_2 in the aqueous phase using the correlation derived with the Speedy–Angell power-law approach by Lu et al. (2013). The model does not consider the ion diffusion of other components in the aqueous phase, given their negligible diffusion rates compared to water and CO_2. On the other hand, the diffusion coefficients in the supercritical phase were calculated based on the Chapman-Enskog theory for gases (Hirschfelder et al., 1949). Only H_2O and CO_2 coefficients are calculated, given that the other components (salts and calcite) are not present in this phase.

We study four main trapping mechanisms for CO_2: structural and stratigraphic trapping, residual trapping, solubility trapping, and mineral trapping. To determine the amount of CO_2 structurally trapped, we tracked the supercritical CO_2 flow rate in each grid cell within the model. If this flow rate is less than a threshold value, we consider the CO_2 virtually trapped. We computed the amount of CO_2 stored in residual trapping from the endpoint saturations (the critical free-phase saturation) of the saturation functions that determine the relative permeability and capillary pressure profiles. The amount of CO_2 dissolved

Table 1
Reservoir parameters for the base-case model.

Parameters	Values
Reservoir temperature, °C	71
Reservoir depth, m	3,650
Initial reservoir pressure, MPa	40
Aquifer brine saturation	1
Initial supercritical CO_2 saturation	0
Average permeability, mD	3.02
Average porosity, %	9
Facies fraction	Sand (32%), Fine sand (25%), Shale (43%)

Table 2
Fluid parameters for the base-case model.

Parameters		Mole fractions
Initial aquifer composition	H_2O	0.96
	CO_2	0
	NaCl	0.025
	$CaCl_2$	0.007
	$CaCO_3$	0.008
Diffusion coefficients in aqueous phase, m^2/d	H_2O; CO_2	5.0×10^{-4}; 3.9×10^{-4}
Diffusion coefficients in supercritical phase, m^2/d	H_2O; CO_2	3.0×10^{-3}; 6.1×10^{-3}

is governed by its solubility in the aqueous phase and is affected by pressure, temperature, and the aqueous phase composition. Here, we calculated the amount of CO_2 dissolved based on the phase splitting model by Spycher and Pruess (2005) described previously. Lastly, the contribution of mineral trapping, the slowest and the most permanent form of trapping gets included in this study. Underestimation of the mineral trapping may occur given the time frame (100 years of injection and 200 years post-injection periods) and the simplified chemical system adopted in our simulations.

Now, let us delve into the numerical simulation and the experimental design used in this study. We used the multicomponent carbon-storage module of the commercial ECLIPSE[1] industry-reference reservoir simulator (Schlumberger, 2020) to model the dynamics of CO_2 injection into saline aquifers.

2.2. Design of experiments

We performed DoE to investigate the dynamics under various subsurface and operational conditions for a carbon-sequestration well in saline aquifers to examine well-based monitoring and address our questions critically. The previous section discussed constructing the base-case geological, petrophysical model, fluid, and rock-fluid characterizations. The main reservoir parameters for the base case include an average porosity of 9% and permeability of 3.02 mD, with a facies distribution of sand (32%), fine sand (25%), and shale (43%). The caprock and the baffle zone comprise shale (90 and 75%, respectively), and the remaining facies are fine sand. The pressure and temperature gradients for the base-case brine were 10.9 kPa/m and 0.019 °C/m, respectively.

Additional reservoir parameters and relevant fluid properties, such as initial fluid composition and diffusion coefficients for the liquid and supercritical phases, appear in Tables 1 and 2. Furthermore, to capture the capillary effects on the transport and trapping of CO_2 and the displacement behavior of the various phases, we implemented multiple relative permeabilities and capillary pressure curves for each facies present in the model. The saturation function endpoints for the facies of interest, including sandstone, shaly sand, and shale, appear in Table S1 in the supplementary file.

We used a single vertical injection well completed in the 3635–3665 m interval in the geological model's lower zone for all the scenarios investigated. In the base-case model, CO_2 in the gaseous phase (at the surface condition) is injected for 100 years at a surface target rate of 2,375 t/yr and a limiting bottomhole injection pressure of 55 MPa, with additional 200 years of post-injection for a total of 300 years of simulation.

For the DoE, we considered uncertain variables encompassing geological characterization, such as the distribution of geological bodies and facies, and petrophysical parameterization, such as porosity, permeability, permeability anisotropy of the aquifer and the caprock. Operational constraints include injection rates, bottomhole pressures, and aquifer fluid composition. Table 3 lists all the uncertain variables and their ranges of variation.

Some of the uncertain parameters are in tabular or grouped format. These include the initial fluid composition comprising a set of component mole fractions, the fluid-mobility reduction due to solid adsorption on rock surfaces, and the saturation tables. The effect of the fluid composition was studied via nine unique sets, as shown in Table S2 (supplementary material). Three sets of fluid-mobility reduction due to solid adsorption on rock surfaces were used (shown in Table S3). Similarly, multiple saturation tables with relative permeability and capillary-pressure characteristics aided in representing various rock facies included in the analysis.

As for the sampling in the DoE, we implemented two sampling designs. The first one uses extreme values (the minimums and the maximums) in the well-known Plackett-Burman design (Plackett and Burman, 1946). In contrast, the other sampling design is a space-filling Latin-hypercube design (McKay et al., 2000). We formulated 500 case scenarios, 21 from the Plackett-Burman design and 479 with Latin-hypercube samples.

We defined two regions based on the radial distance from the injection well to facilitate the analysis of the plume evolution and aquifer properties near and away from the wellbore. The wellbore region, region 1, comprises the well up to 150 m. We deliberately avoided local-grid refinement in models because our investigation focuses on the dynamics away from the well than those in the wellbore region.

3. Well-based monitoring: key questions

As mentioned, this study addresses critical questions relating to passive well-based monitoring for carbon sequestration in saline aquifers. These questions are: (1) Which plume characteristics can we monitor using well-based variables? (2) Can any well variables provide insights into the temporal evolution of the plumes? (3) How representative are the near-wellbore fluid properties of the plume average properties? (4) How sensitive are the well variables to different plume dynamics metrics? In the following, we present detailed analytics to address these questions.

3.1. Which plume characteristics can be monitored?

One would want to determine several plume characteristics for proper carbon sequestration operations. However, it is not practical to examine and monitor all the parameters and variables related to the CO_2 plumes given the finite resources, inadequate knowledge of the aquifer architecture, and limited access to data and measurements. In this study, we focused on the following plume characteristics:

- The radial (lateral) extent of the plumes
- The vertical spread of the plumes
- The temporal evolution of the plumes

We first explored if we could ascertain the spatial characteristics of the CO_2 plumes using well-based monitoring. To this end, we investigated several spatial characteristics of CO_2 plumes. We follow the plume definitions described by Zapata et al. (2020). The CO_2 plumes are defined based on CO_2 dissolved in the aqueous phase, pH change, presence of CO_2 in a supercritical state, and solid-phase saturation changes

---

[1] Mark of Schlumberger

Table 3
Variables and their range used for uncertainty and sensitivity analysis.

	Minimum	Base	Maximum
Percentage of sand channels	11	14	17
Percentage of shaly sand bodies	15	18	20
Major direction of continuity in porosity variogram (sand facies), m	700	1,000	1,500
Minor direction of continuity in permeability variogram (shale facies), m	1,800	2,500	3,000
Porosity multiplier	0.5	1	2
Permeability in X-direction multiplier	0.1	1	10
Permeability vertical anisotropy	0.01	0.1	1
Permeability horizontal anisotropy	0.25	1	4
Caprock vertical permeability multiplier	0.01	0.1	1
Baffle vertical permeability multiplier	0.01	0.1	1
Initial reservoir pressure multiplier	0.83	1	1.17
Injection rate, t/dd	30	65	100
Maximum bottomhole pressure, MPa	51	55	60
Rock compressibility, 1/MPa	6×10^{-5}	1.2×10^{-4}	2.4×10^{-4}
Water and supercritical CO_2 phase saturation tables per rock facies	1	2	3
Fluid-mobility reduction due to solid adsorption (tables)	1	2	3
Initial composition (tables)	1	5	9

due to dissolution or precipitation. Fig. 2 shows the plumes' average radial extent (lateral extent) profiles against CO_2 injected. For brevity, we exclude the explanations of the observed plume-geometry metrics and the calculation in this manuscript. Interested readers may refer to our previous manuscript (Zapata et al., 2020). The radial dimension of the plumes based on CO_2 dissolved in the aqueous phase (Fig. 2a) is typically more extensive than those for plumes based on other metrics (100 to 700 m). Aqueous CO_2 spreads laterally into the reservoir due to advective and diffusive flows in the aqueous phase, as supported by the aquifer's connectivity.

In contrast, the plume's shortest radial extent can be observed based on CO_2 in the supercritical phase (Fig. 2b) with up to 400 m into the reservoir. Due to buoyancy and gravitational forces, the supercritical CO_2 travels more vertically than propagates laterally. The poor petrophysical characteristics, namely, low porosity and low permeability of the aquifer models, also contributed to the limited lateral propagation of the supercritical CO_2.

Additionally, the multiphase effect may impede the reach of the supercritical free phase. In other words, supercritical free-phase CO_2 can only become mobile once the critical saturation exceeds. As the CO_2 gets injected, the supercritical free phase accumulates near the wellbore and displaces the aqueous phase. This step, in turn, is responsible for the shift in radial extension observed in both the CO_2 dissolved (Fig. 2a) and the pH changes (Fig. 2c) measured in the aqueous phase. Because the aqueous phase already exists in the aquifers in the mobile state, the initial movement of the aqueous phase does not get throttled by the multiphase effect. This phenomenon manifests in the linearity relationship (in the log-log scale) between the radial extent and the amount of injected CO_2, which develops at a much earlier stage for plumes based on CO_2 dissolved and pH changes. A similar linearity relationship for the supercritical free phase develops later.

The radial extent of the plume regions where pH changes occur due to CO_2 injection ranges from 100 to 500 m. Some cases exhibit additional growth, up to 900 m, even after the injection stops (Fig. 2c). The pH changes are related to the presence of CO_2 in the aqueous phase and the buffering effects of calcite dissolution events resulting from the acidic conditions. The latter events occurred in the region with radial extension presented in Fig. 2d from 50 to 500 m into the reservoir. The fluctuations observed in each scenario profile are due to variations in the occurrence of the reactions. Dissolution and precipitation can co-occur at different parts of the reservoir. A more satisfactory grid resolution can help mitigate the observed variations.

We also studied plume growth with depth. Fig. 3 presents the plume's radial extent of depth profiles for all cases at two contrasting times: after 100 years (when injection ceases) and 200 years from the end of the injection period. We present only the profiles of the plumes defined based on CO_2 dissolved in the aqueous phase. Each curve (some not discernable) represents a scenario from the design of experiments; they are colored by the total CO_2 injected. The dimensions and shapes of the observed plume fronts depend on the fluid properties and composition, the aquifer's petrophysical and chemical characteristics, and the CO_2-brine-rock interactions. We highlight the CO_2 transport characteristics in the aqueous phase in Figure 3. The plume fronts for the CO_2 in the aqueous phase tend to progress more laterally (below the injection depth) for both times. One can attribute this behavior to the structural connectivity architecture of the aquifer and convective mixing resulting from the brine density increment due to CO_2 diffusion. In this context, Hassanzadeh et al., 2005 also observed convective flux and highlighted the role of convective instability in CO_2 solubility.

An important observation from the radial extent profiles is the linearity of the radial extent profiles and cumulative injected CO_2 in the log-log scale. This reality implies that the injected CO_2 can determine the plumes' average radial extent with some margin of error. In addition, the prominence of lateral growth compared to vertical growth for all the cases studied highlights the role of structural connectivity and advective transport in plume evolution.

3.2. Which fluid properties provide insights into temporal plume evolution?

A natural question arises: Which properties would be good to monitor and use in inferring the characteristics of the CO_2 plumes? Complexities occur due to the dynamic nature of the processes involved and the variation in the fluid properties. The aqueous phase properties evolve with CO_2 injection and time due to interactions between the fluids and rocks. The chemical characteristics of the brine can enhance (or impair) the CO_2 dissolution and its reaction with other species present in the aqueous phase, resulting in more (or less) solubility and mineral trapping of CO_2. In this study, we considered pH, pH changes (relative to initial pH), aqueous phase density, and species activity in the aqueous phase would be appropriate to deduce information on the CO_2 plumes. Besides, suitable sensors can monitor these properties within the injection well. Note that this manuscript does not address the intricacies of the sensing techniques and current capabilities. At this stage, we presume it is possible to sense and monitor these properties in the downhole condition. We critically examine these "monitorable" variables following that assumption.

We first explored how these variables are related to each other. Fig. 4 shows the pair-wise cross-plots amongst these variables investigated after 300 years for all the scenarios. The cumulative CO_2 injection colors the cross-plots. We observed various interesting signatures among the fluid properties. The pH cross-plots revealed two different clusters that appear depending on the presence or absence of aqueous calcite in the

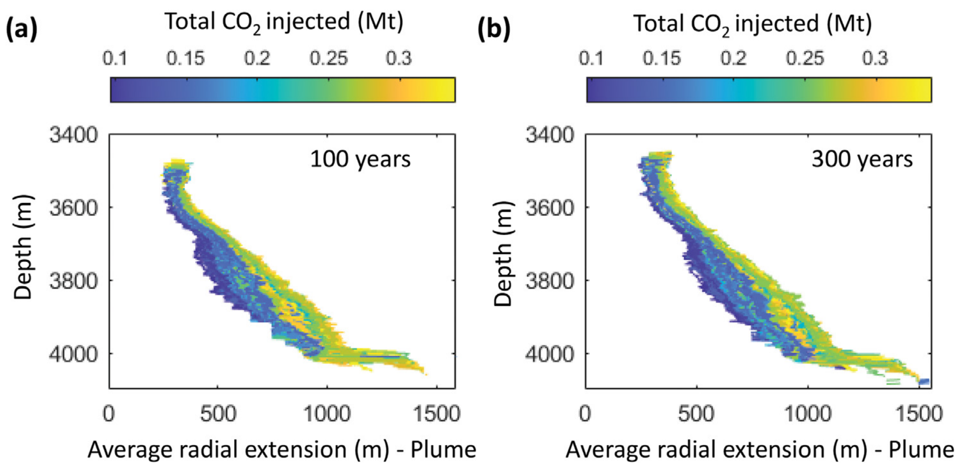

Fig. 3. Depth profiles of plume radial extension for all cases (a) after 100 years and (b) after 300 years. The red line indicates the injection depth. Here, plumes are defined based on CO_2 dissolved in the aqueous phase.

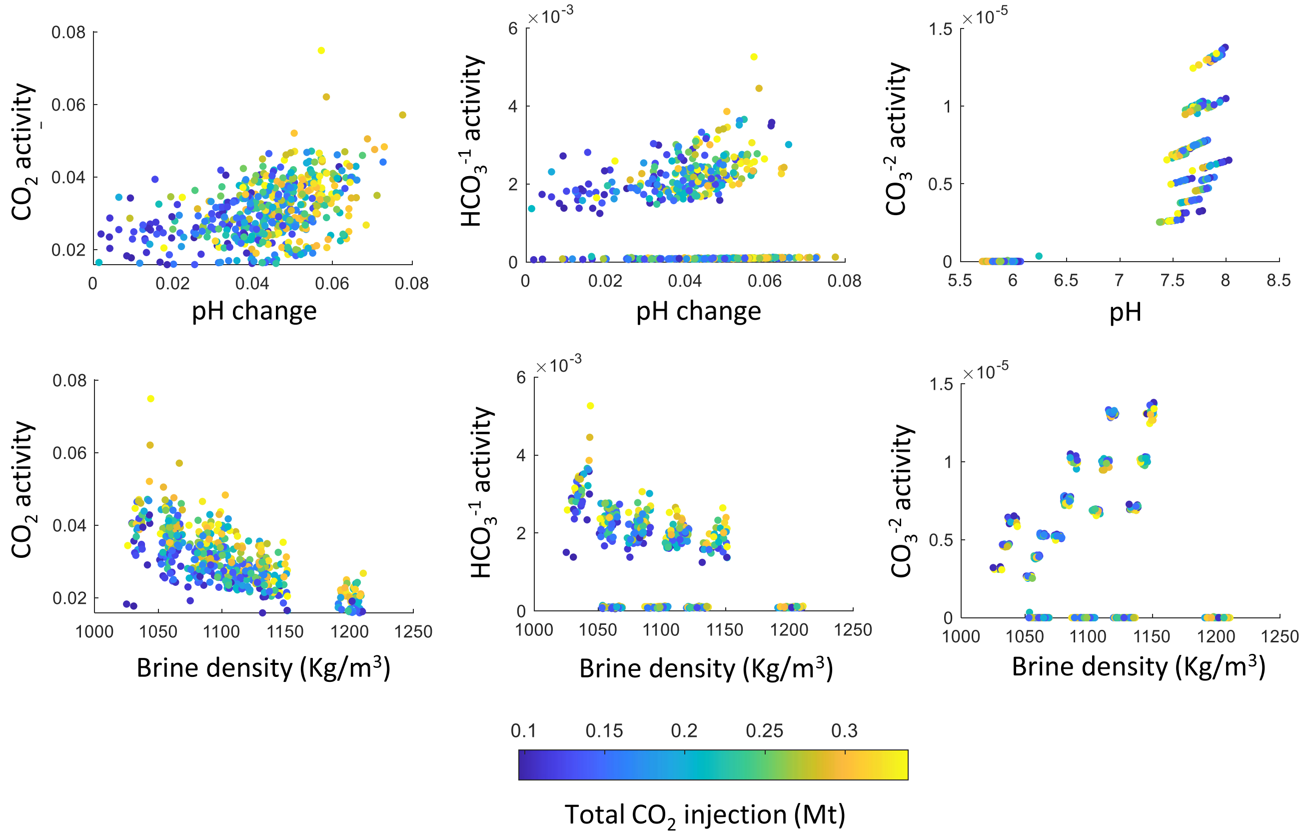

Fig. 4. Pair-wise cross-plots amongst the monitorable fluid properties for all the scenarios after 300 years (that is, 200 years after the injection stoppage). The fluid properties are averaged over the plume based on the plume defined by the CO_2 in the aqueous phase. Each data point represents a scenario from the design of experiments and is colored by the total CO_2 injected. The top row presents the cross-plots of the pH change with the CO_2 aqueous speciation components activity ($CO_{2(aq)}$, HCO_3^{-1} and CO_3^{-2}). The subsequent row of subplots represents the cross-plots against brine density for the aqueous speciation components.

initial aquifer fluid composition. Initial calcite in the aquifer fluid leads to fundamental (alkaline) pH values compared to acidic values in the absence of calcites in the initial composition. A positive correlation between the pH change and the activities of aqueous CO_2 and HCO_3^{-1} emerges, emphasizing the influence of pH behavior in the speciation of CO_2 inside the aquifer brine. The initial fluid composition is also a primary factor determining the brine density, which increases with salinity.

Calcite's initial presence in the brine is evident in its density behavior and relationship with the CO_2 solubility. We noted a positive correlation between density and the activity of CO_3^{-2}, which is mainly related to the initial composition. Here, CO_3^{-2} activity positively correlates with brine density, but only when the calcite is initially present in the aqueous phase. The carbonate ion activity depends on calcite dissolution and is related to an increment in Ca^{+2} activity; given the sizeable molecular weight of Ca^{+2}, the high CO_3^{-2} activity relates to high-density brine. In contrast, CO_2 and HCO_3^{-1} species activities negatively correlate with the brine density. As expected, CO_2 will have higher activity in the rarefied aqueous phase than in the denser phase. Besides, the speciation of CO_2 into HCO_3^{-1} is positively correlated, and their activities increase with continued CO_2 injection.

The cross-plots in Fig. 4 also reveal the redundancy or complementary nature of the relationships amongst the monitorable variables. To

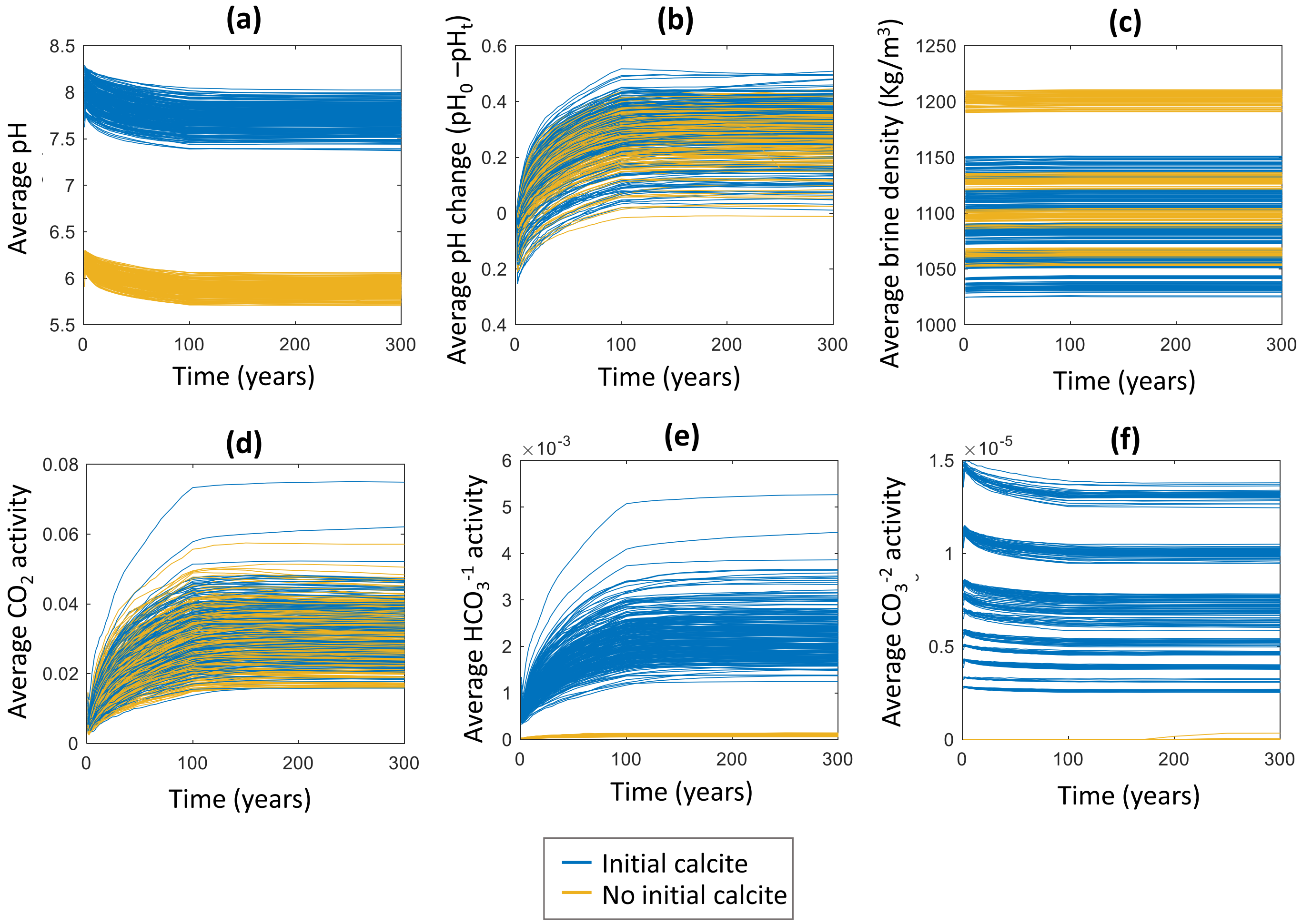

Fig. 5. Fluid properties evolution with time for all case scenarios (a) pH, (b) pH change, (c) brine density, (d) aqueous CO_2 with time, (e) aqueous HCO3 with time−, and (f) aqueous CO3−2 with time.

that end, we found that all these variables carry additional information other than the $HCO_3{}^{-1}$ and CO_2 activities pair. This pair has a strong positive correlation. In other words, knowledge of $HCO_3{}^{-1}$ activities may not add value to the study if we already know about CO_2 activities.

We now explore the temporal behavior of the fluid properties. We evaluated their time evolution, considering the role of the initial calcite presence in the aquifer fluid.

Fig. 5 shows each property—average pH, pH change, brine density, and the activity of aqueous CO_2, $HCO_3{}^{-1}$, and $CO_3{}^{-2}$—as a function of time for all the cases studied. The pH decreases with time as a function of the CO_2 injected. Again, we identify two clusters marked by the initial presence of calcite in the aqueous phase (Fig. 5a). The initial calcite content affects the pH changes around the injection well and into the reservoir. Similar evidence of pH behavior associated with calcite pH buffering has appeared in reactive transport simulations of carbonated aquifers (Lagneau et al., 2005). The effect of the original composition disappears when we analyze the pH change (Fig. 5b). In this case, more considerable changes in pH occurs, especially during the injection phase. A negative pH change appears initially; the initial readjustment of minerals can explain the solid phase, increasing the pH. A decreasing pH follows this step due to CO_2 injection that dissolves into the aqueous phase.

As for brine density, strong dependence on the initial calcite content becomes obvious. The brine density profiles show minor change with time (Fig. 5c). The CO_2 and $HCO_3{}^{-1}$ activities increase with time because of increased injected CO_2 (Fig. 5d and Figure 5e) and reveal similar trends. Both are stoichiometrically interrelated, as shown in Eq. 1 in Zapata et al. (2020). However, the activity of $CO_3{}^{-2}$ is not only dependent on the CO_2 injected but also affected by the calcite dissolution and the initial fluid composition. The characteristic trends of different initial compositions are apparent in Fig. 5f. Overall, the activity of this ion decreases with time.

Furthermore, the equilibrium of the components in the aqueous phase from CO_2 speciation is highly dependent on the pH, as Fig. 5 displays. The dominant species from CO_2 dissolution at lower pH is the aqueous CO_2. This observation explains the higher activities, given that the chemical system exhibits a trend of pH decline.

We noted that pH and pH change carry helpful information on the plume dynamics from the previous discussion. Fig. 6 explores the variation in the aqueous phase pH and pH change and their relationship with the spatial plume characteristics, the radial extent, and the aspect ratio. In Fig. 6, each datum point represents the average pH change within the CO_2 plume at the end of 300 years for a given case from the DoE run conducted. Note that we examined the 100-year CO_2 injection and 200-year post-injection periods. The plume radial extent has a strong semblance in pH change and aspect ratio but is reciprocally based on Figs. 6a and 6b. Insignificant changes in pH correlate well with higher plume aspect ratios and low total CO_2 injected, which means shorter plumes in the vertical direction exhibit less relative pH change. In other words, more extensive plumes in the horizontal direction experience more significant changes in pH.

We also explored the relationship of brine density with plume properties. In this case, the plume dimensions, such as radial extension and aspect ratio, do not exhibit noticeable correlations with the aquifer brine

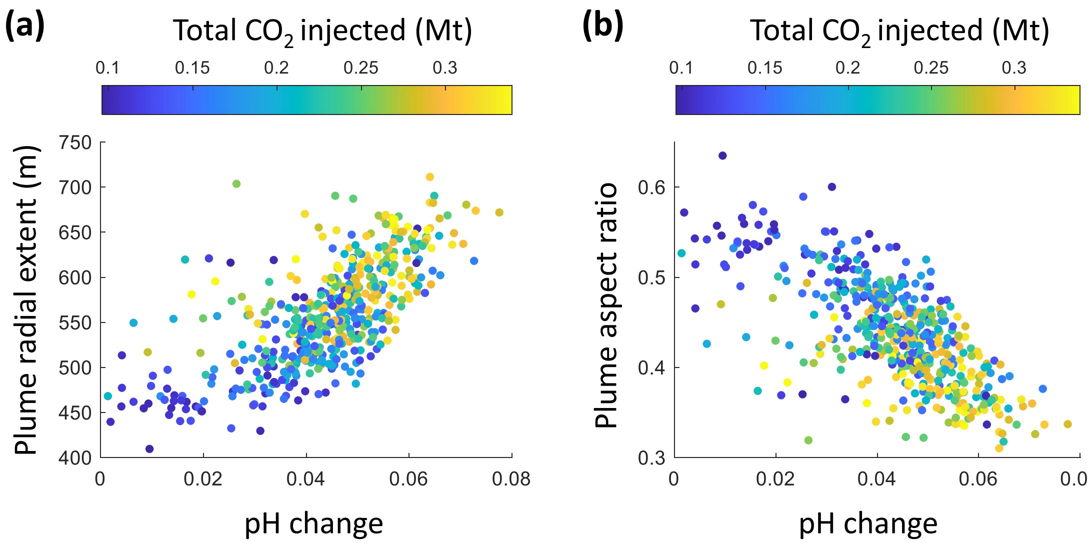

Fig. 6. Aquifer fluid pH behavior for all case scenarios after 100-year injection and 200-year post-injection periods: (a) pH with plume radial extension and total CO_2 injected; (b) pH change with plume aspect ratio and total CO_2 injected.

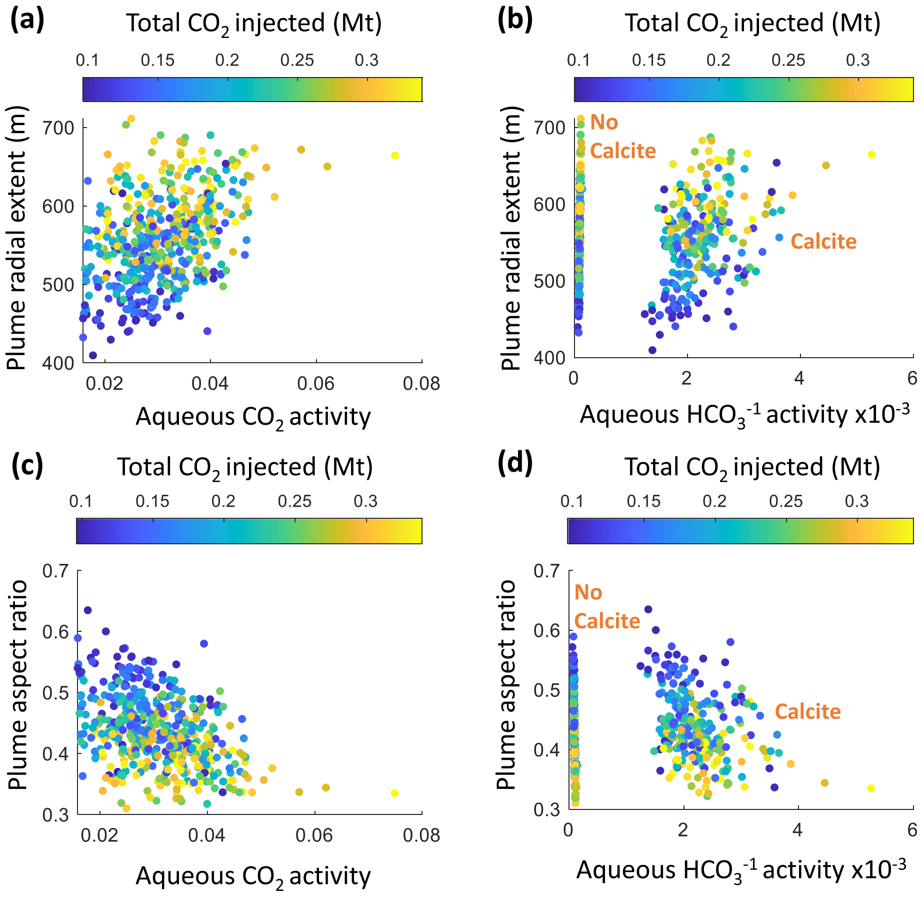

Fig. 7. Carbonate species relation with plume dimensions. Plume radial extension with (a) aqueous CO_2 and (b) HCO3−1 activities, and plume aspect ratio with (c) aqueous CO_2 and (d) HCO3−1 activities.

density. Brine density variations were related to the initial brine composition but not the plume evolution. Larger densities coincide with a higher content of dissolved solids, such as NaCl, $CaCl_2$, and $CaCO_3$. The brine density does not exhibit a direct influence on the plume size. However, the distribution of CO_2 in distinct trapping mechanisms, such as solubility trapping, is correlated with the brine density, influencing the plume extension indirectly.

Can we use the activities of carbonate ions (aqueous CO_2, HCO_3^{-1}, and CO_3^{-2}) to understand the CO_2 plumes? Fig. 7 attempts to address this question. More significant CO_2 and HCO_3^{-1} activities are associated with lower aspect ratios, as shown in Figs. 7c and 7d. Therefore, as Figs. 7a and 7b display, they relate to laterally deeper plumes (more significant radial extension) into the formation and higher calcite content.

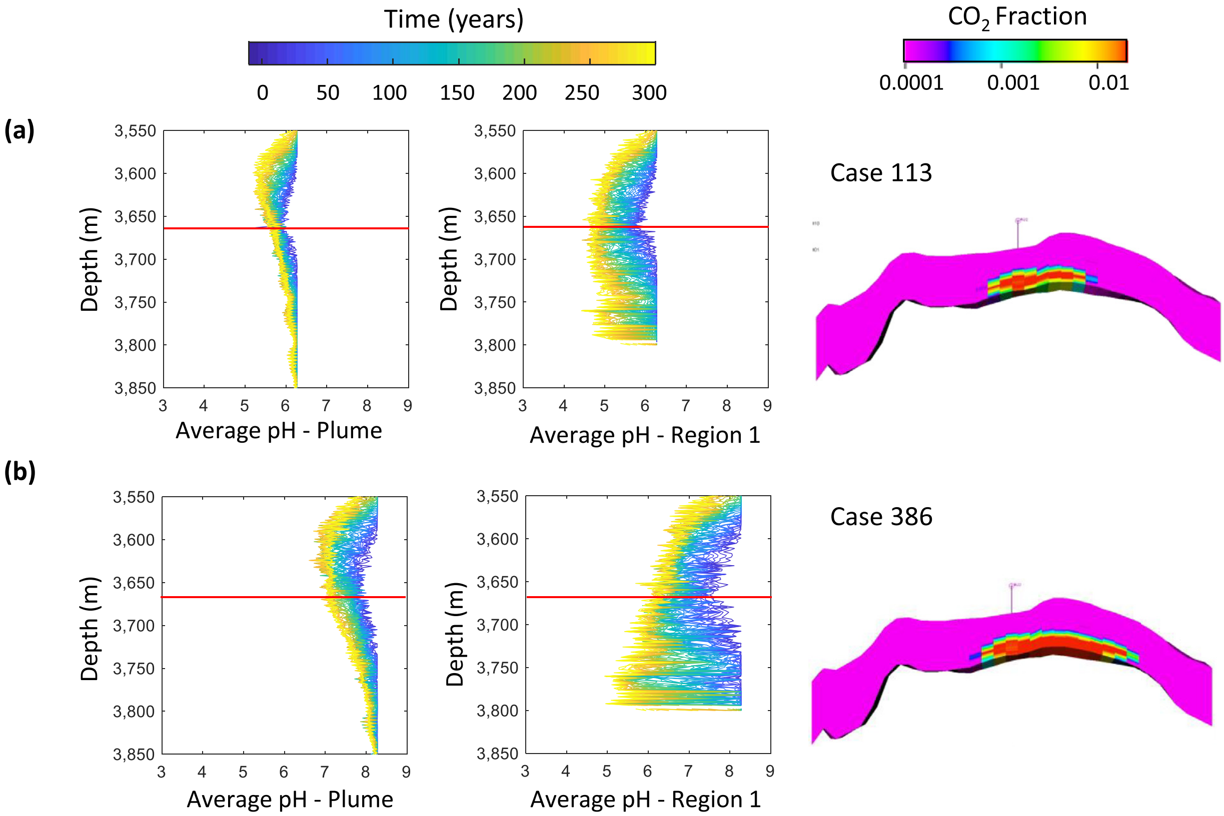

Fig. 8. pH gradient evolution for both the Plume region and Region 1 (near the well) for selected cases (a) case 113 and (b) case 386. The red line indicates the injection depth. On the right a cross-sectional image of the simulated plume after 300 years.

On the other hand, the $CO_3{}^{-2}$ activity does not show any evident correlation with the plume aspect ratio or radial extension, as the initial fluid composition influences it, particularly by the calcite content. This signature suggests that the initial composition of the brine has a role in how the aqueous species interact. The plume growth relates to the activity of aqueous CO_2 and $HCO_3{}^{-1}$. However, other interactions of $CO_3{}^{-2}$ with calcite and calcium ions will affect the movement of these ions.

To recap, evaluating the selected fluid properties' interactions and relationships with the CO_2 plume dimensions confirms that not all the fluid properties carry similar information content. The initial calcite presence in the aqueous phase determines the relationships for many of these variable pairs. The pH changes can be more informative about the speciation and activities of CO_2 and $HCO_3{}^{-1}$ in the aqueous phase and can correlate with the plume aspect ratio and radial extension. In contrast, the brine density and $CO_3{}^{-2}$ activity (not shown in the above figure due to brevity) do not significantly affect the plume dimensions, given that the original brine composition influences them. As expected, the amount of CO_2 injected plays a relevant role in the brine properties variation.

3.3. How representative are near-well properties of the average plume properties?

One of the main challenges in determining aquifer dynamics is the lack of information and proper characterization of the rocks and fluids and their subsurface interactions. We discussed which plume characteristics and which properties we could monitor above. The reach of downhole monitoring sensors can only be a few meters into the reservoirs from the wellbore. Then, a natural question arises: How representative are the near-well properties of the plume average properties? We turn our attention to this problem here.

We used two regions for this analysis, namely region-1 and the plume region. Region-1 represents the near-well region (within 150 m from the well), and the plume region encompasses the aquifer volume of CO_2 in the aqueous phase. Note that the radial extension of the plume region varies, as shown previously in Fig. 3. We computed the average variation with depth and time of the properties of interest within these two regions. The selected properties included are pH, brine density, and various carbonate species' activity for brevity.

First, we examined the variations in pH in region-1 and the plume region. Fig. 8 shows the depth profiles of average pH over time for selected cases in both regions. Table 4 summarizes petrophysical properties and fluid and operational parameters for these cases. On the right in Fig. 8, we included cross-sectional views showing the plume shape at the end of 300 years. In general, the near-well pH depth profiles can only capture the average plume profiles above the injection depth in most cases. However, below the injection depth, this resemblance disappears in most cases. More significant pH drops can occur at depths where the plume grows farther away from the well into the aquifer (cases with more considerable radial extension, such as case 386).

The reservoir connectivity architecture plays a substantial role in the displacement front below the injection depth, as the CO_2 plume propagates more laterally into the formation. At the same time, some transverse (vertical) displacement occurs because as CO_2 dissolves into water, the brine becomes denser and generates a downward flow. Therefore, the downward flow induces a higher pH reduction below the injection depth. The other observation is that the plume-average profiles are somewhat subdued compared to those in the near-well region. This reality occurs due to the most active dynamics that unfold near the well. The brine's initial composition also affects the pH's initial depth profiles. An important observation is that the temporal change in the depth profile of the pH provides information about the broader trends inside the plume region, as Fig. 8 displays.

Table 4
Petrophysical, fluid and operational parameters for cases 113 and 386.

Property	Case 113	Case 386
Average porosity, fraction	0.18	0.07
Average permeability in X-direction, mD	24.7	17.3
Average permeability in the seal formation, mD	1.6×10^{-2}	6.1×10^{-3}
Permeability vertical anisotropy	0.16	0.25
Permeability horizontal anisotropy	2.66	2.5
Rock compressibility, 1/bar	6.7×10^{-5}	8.4×10^{-5}
Reservoir pressure, MPa	42.8	43.6
Bottom hole pressure, MPa	56.5	55.8
Average injection rate, t/y	2484	3986
CO_2 diffusion coefficient in supercritical phase	6.5×10^{-3}	6.9×10^{-3}
H_2O diffusion coefficient in supercritical phase	3.2×10^{-3}	3.4×10^{-3}
CO_2 liquid diffusion coefficient, m^2/d	4.5×10^{-4}	3.9×10^{-4}
H_2O liquid diffusion coefficient, m^2/d	5.7×10^{-4}	4.9×10^{-4}
Maximum capillary pressure in shale, MPa	5.0	4.5
Maximum capillary pressure in shaly sand, MPa	2.2	2.5
Maximum capillary pressure in sand, MPa	0.8	0.8
Residual CO_2 saturation for shale	0.271	0.328
Residual CO_2 saturation for shaly sand	0.196	0.138
Residual CO_2 saturation for sand	0.02	0.02
Irreducible water saturation for shale	0.36	0.32
Irreducible water saturation for shaly sand	0.15	0.15
Irreducible water saturation for sand	0.08	0.08
CO_2 rel. permeability at residual water saturation for shale	0.65	0.6
CO_2 rel. permeability at residual water saturation for shaly sand	0.75	0.8
CO_2 rel. permeability at residual water saturation for sand	0.95	0.95
Water rel. permeability at residual CO_2 saturation for shale	0.5	0.6
Water rel. permeability at residual CO_2 saturation for shaly sand	0.3	0.25
Water rel. permeability at residual CO_2 saturation for sand	0.63	0.63
Salinity, kppm	186.0	166.3
Supercritical phase density, kg/m^3	822	867
Initial $CaCO_3$ mole fraction	0	0.019
Initial pH	6.1	8.1

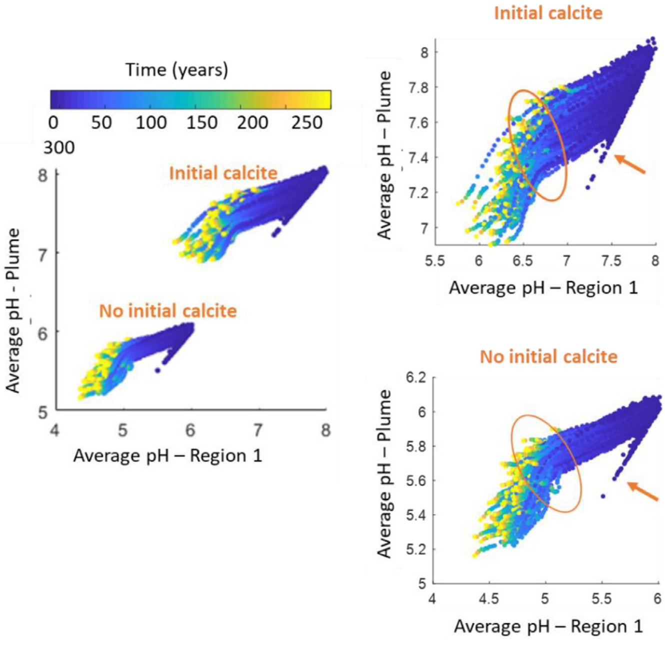

Fig. 9. Cross-plots between the average pH of the entire plume and Region-1 (near-well) for all case scenarios over time.

Next, we investigated how the near-well and plume average pH values are correlated. Fig. 9 presents cross-plots of the average pH for the entire plume and Region 1 (near-well) for all times and scenarios investigated (from the DoE). Each data point in Fig. 9 represents the corresponding near-well and plume average pH values for a given case at a given time step. For brevity, we only present the plume defined by CO_2 dissolved in the aqueous phase. As expected, early-time near-well and plume-average pH correlate well because the plume initially remains confined to the near-well region. As time progresses, the plume-average pH values deviate from the near-well pH values and become slightly more prominent.

Another signature observed in some cases is an initial increment in pH (as indicated by the orange arrows in Figure 10), followed by a reduction of pH characterized by the two different slopes previously mentioned. This behavior is apparent irrespective of the initial calcite content, which we can explain by the initial interaction of other salts and ions in the aqueous phase with the injected CO_2. This interaction results from the initial precipitation of salts, and for cases with calcite content, in the initial dissolution of calcite that buffers the pH.

Similarly, we analyzed the near-well and plume average brine density and the activities of CO_2 in an aqueous phase and the carbonate ions CO3−2 for different cases. The brine density in this study is based on pure water density and corrected for the presence of salts and dissolved CO_2, allowing for a more accurate prediction of the density variations. CO_2 tends to increase the brine density. Even minor changes in density can affect the dissolution rate of CO_2 as the instability created may induce advective-diffusive mixing and enhance CO_2 dissolution. In Fig. 10, we observe a modest variation in the depth profiles of brine density in the near-well and plume average. Density increases with time as more CO_2 gets injected and dissolves into the aqueous phase, and the most considerable variations occur around the injection depth and near the well. However, unlike the pH, the density depth profiles do not reflect the shape of the CO_2 plumes.

Fig. 11 presents the depth profiles of near-well and plume average movement of CO_2 in the aqueous phase over time for selected cases. The CO_2 effective concentration (activity) in the plume region displays similar patterns as the plume shape itself, as the effective concentration of CO_2 in the aqueous phase mostly correlates to the injected CO_2 (given the initial composition of the brine considered). For example, cases with higher injection rates, such as case 386, show higher variation with depth and reach higher concentrations above the injection point. The near-well activity of CO_2 exhibits a more homogeneous growth for all cases. Overall, there is an evident correspondence between the

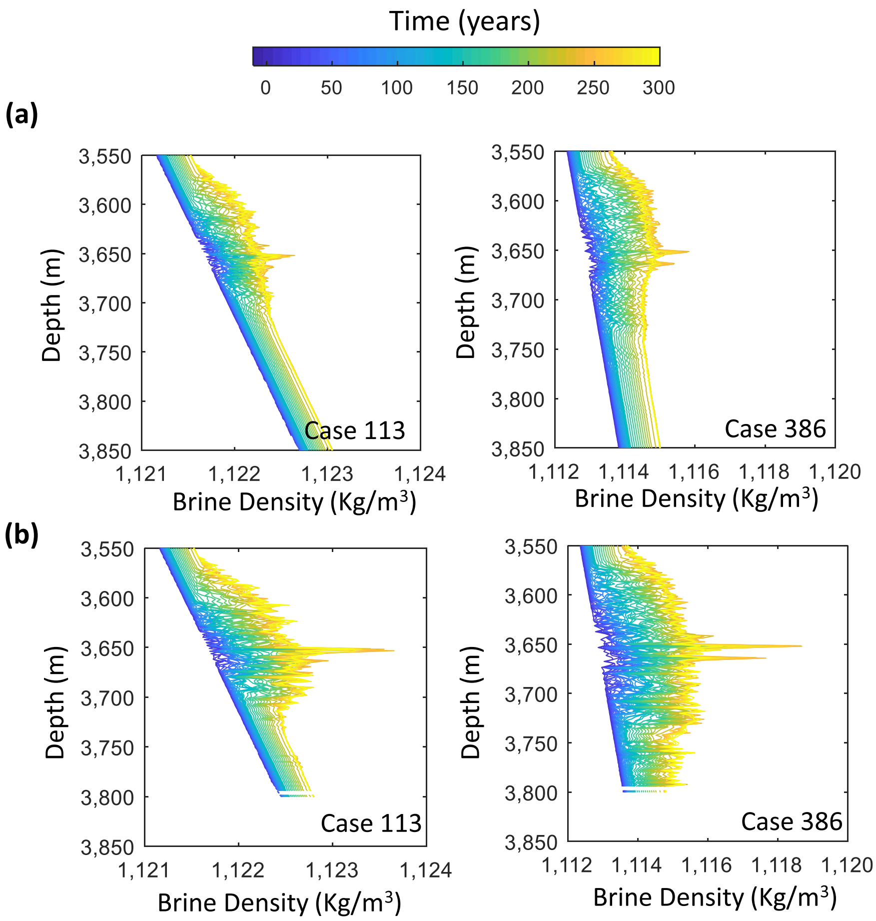

Fig. 10. Depth profiles of brine density and their temporal evolution for the plume region and region 1 (near the well) for selected cases (a) 113 and (b) case 386.

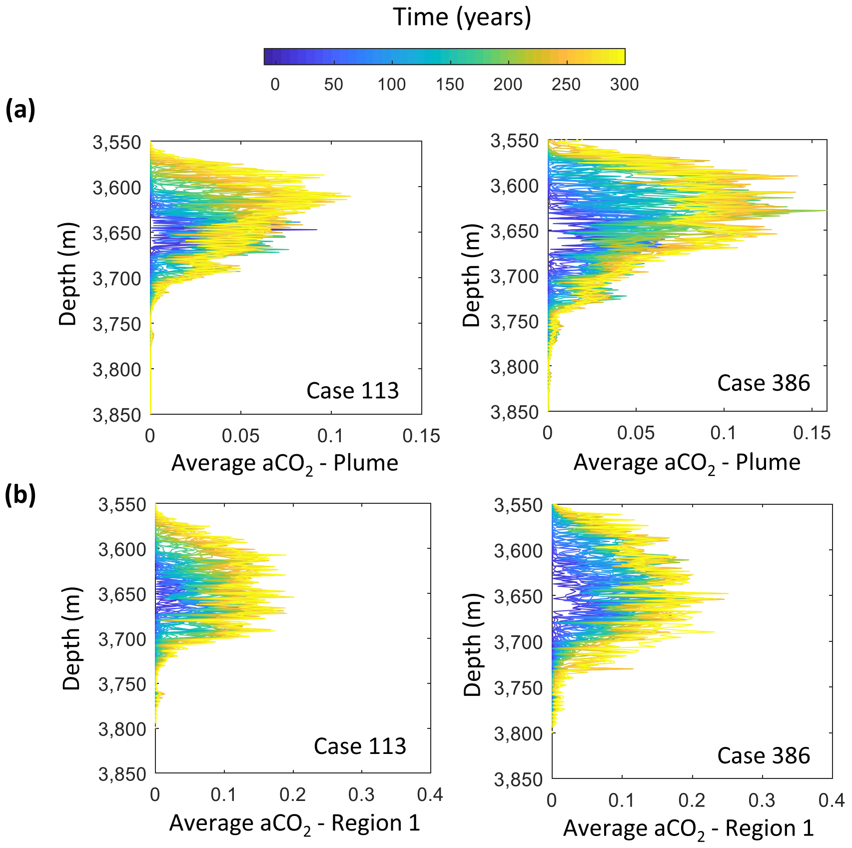

Fig. 11. Depth profiles of the aqueous CO_2 activity and their temporal evolution for both (a) Plume region and (b) Region 1 (near-well). Selected case scenarios: case 113 and case 386.

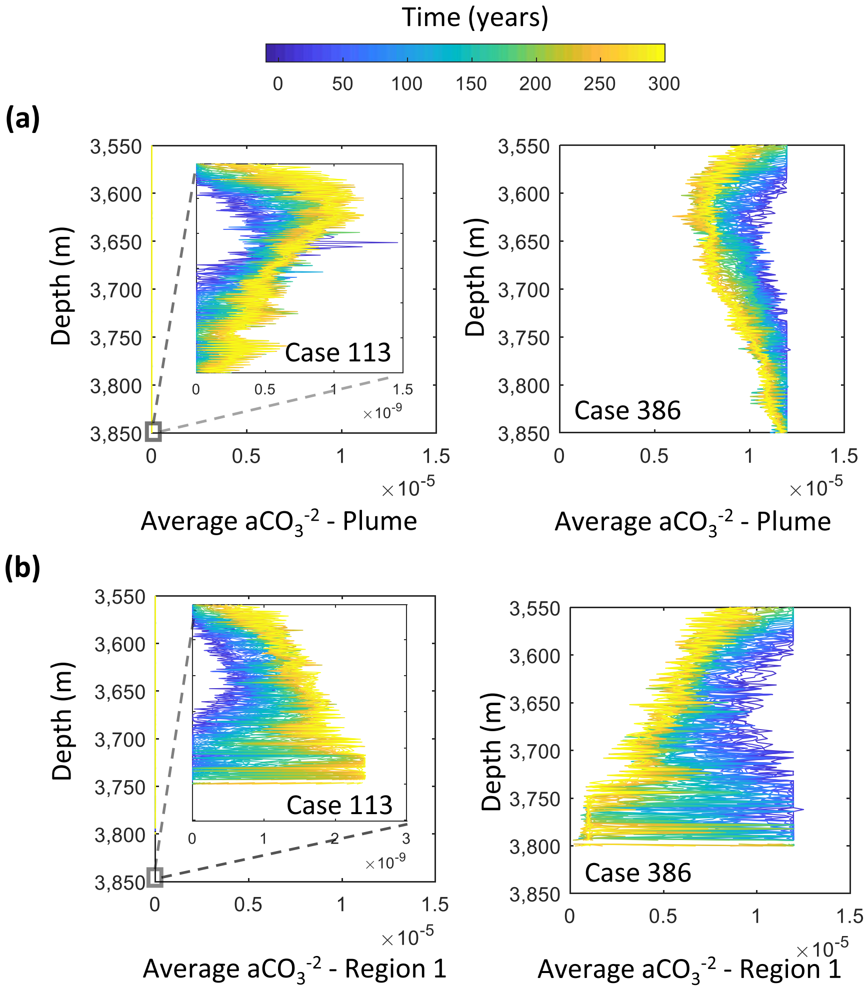

Fig. 12. Depth profiles of the activity in the aqueous phase of CO3−2 and their temporal evolution for both (a) Plume-region and (b) Region 1 (near-well). Selected case scenarios: case 113 and case 386.3.4. How sensitive are plume characteristics to the well-based properties monitored?

depth profiles of the near-well and plume average aqueous phase CO_2 activity.

Similarly, Fig. 12 shows the depth profiles of CO_3^{-2} activity. The effective concentration of the carbonate ion presents a dissimilar behavior in many cases due to the variations in initial calcite content that affect the initial presence of CO_3^{-2} with depth. In this case, the activity becomes a function of both the injection of CO_2 and the brine composition. For cases with initial calcite concentration, the CO_3^{-2} activity decreased with time, especially at depths where the aqueous CO_2 activity increases due to the speciation equilibration (cases 386) and is influenced by the brine pH. For cases with no initial calcite, minimal changes in the effective concentration of the CO_3^{-2} ion appear (case 113). This observation could very well be due to numerical dispersions. The difference in speciation of CO_2 in the aqueous phase for cases with or without initial calcite content highlights the importance of accounting for relevant minerals to understand the CO_2-brine interaction and the interaction of rock and brine responsible for the precipitation or dissolution of minerals.

The behavior of the parameters explored suggests that the pH gradient analysis and the activity of aqueous species such as dissolved CO_2 and HCO_3^{-1} can provide trends that reflect the plume region's evolution. In contrast, the depth profiles of CO_3^{-2} activity or the variations in brine density could not capture the plume behavior with time or depth.

So far, we have discussed which plume characteristics to monitor, which properties to watch, and how representative the near-well values are to plume average values. Now, we focus on the sensitivity of plume characteristics of the variables that one can monitor. The DoE appeared in Section 2. Using DoE uncertain variables and the simulation results, we perform the sensitivity analysis for the plume characteristics of well-based "monitorable" variables.

First, we explored the influence of various fluid properties, from salinity and pH to the effective concentration of ions in the aqueous phase, on the plume dimensions defined based on CO_2 in the supercritical phase. The characteristics examined include the average height and radial extension, as presented in the tornado charts in Fig. 13. The first observation is that the relative influence of fluid properties on the plume dimensions changes during injection and post-injection periods.

For plume height, the salinity and brine density promote the plume height as they hinder the solubility of CO_2 into the aqueous phase. This effect is also evident based on the plume height's negative correlation with the effective concentration of carbonate ions and the brine pH. Another property affecting the plume height is the CO_2 density. As expected, higher CO_2 density correlates to shorter plumes in the vertical direction. After injection stops, the brine density and CO_2 speciation on the plume height appear to reduce. This observation indicates the lesser dominance of convective flux and buoyancy-driven flow in the post-injection period. However, the prominence of compositional equilibration with molecular diffusion appears in the post-injection period.

The plume radial extension depends on the CO_2 activity in the aqueous phase during the injection period, which correlates with the total CO_2 injected into the aquifer. Brine salinity and density contribute to lateral plume growth positively. Once injection stops, we observe a shift in the main parameters influencing the plume growth, with negligible influence from the CO_2 activity. Salinity and salts, such as $CaCl_2$ (with a more significant atomic number), modestly promote post-injection lateral growth while negatively affecting the pH.

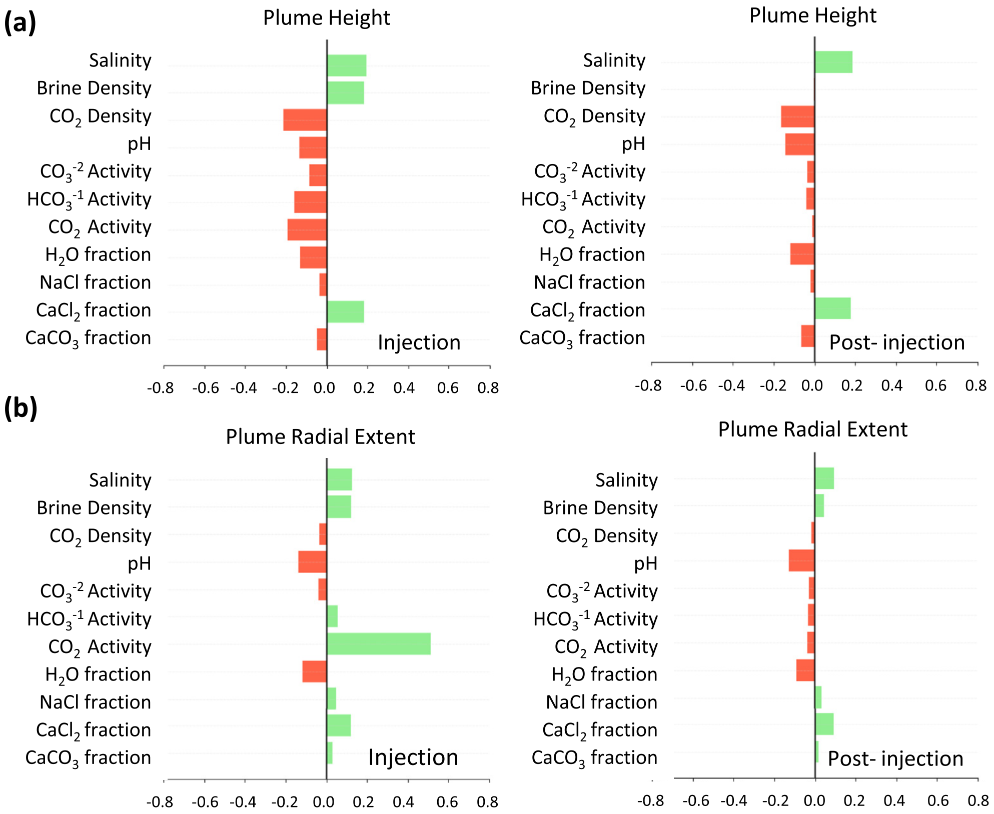

Fig. 13. Relative influence of fluid properties on plume dimensions during injection and post-injection: (a) plume height and (b) plume radial extension.

Next, we examined the relationship of these fluid properties with the distribution of the injected CO_2 into distinct phases and trapping mechanisms. Here, we considered CO_2 mobile in the free phase, CO_2 dissolved in the aqueous phase, and residual CO_2. To compare the amounts stored in each mechanism, we calculated the ratio of CO_2 in those selected trapping mechanisms for the injected CO_2. Fig. 14 shows the tornado plots for the chosen fluid properties' relative contribution to the different trapping mechanisms. Salinity and brine density play an essential role in all the trapping means. Higher salinity and brine density values promote CO_2 in the free phase and are residually trapped, hindering CO_2 solubility. This step is related to salts and calcite in the aqueous phase. The role of brine density and the effective concentration of various carbonate ions get reduced after injection stops for all cases investigated. On the other hand, the brine pH affects the solubility trapping, with negligible effects on other trapping mechanisms.

4. Discussion

Here, we present additional considerations concerning the investigation observations. We address the monitoring of fluid properties and their relationship with the plume evolution, including discussing the limitations of the methodology. Table 5 presents the key questions posed at the study's onset and the lessons learned. The development and implementation pace and success of CO_2 capture and storage technologies depend on predicting, managing, and monitoring changes in the subsurface due to the injection of CO_2. Modeling and simulation of injection, storage, and trapping processes are vital to understanding the behavior and interaction of CO_2 with the minerals and fluids that are part of the aquifer formations. Furthermore, using available monitoring tools to determine and track the plume behavior with time is essential to ensure the integrity and security of CO_2 storage projects. In this study, we aimed to extend the prediction capabilities of geochemical tools by investigating the evolution of fluid properties with time and how they are related to the plume dimensions.

4.1. On fluid properties

We considered five fluid properties for the analysis, namely, pH, brine density, and the activities of CO_2, HCO_3^{-1}, and CO_3^{-2}. Our investigations note that the initial brine composition is essential in evolving the fluid properties evaluated and their interaction with the injected CO_2. In particular, the initial content of calcite affects the brine density, CO_2 solubility, and the solid saturation of the system. We only investigated a subset of possibilities. Therefore, we recommend that the aquifer brine composition and its relationship with different CO_2 trapping and plume growth forms need special attention.

4.2. On near-well vs. plume region monitoring

We know that the well-based sensors can only measure properties a few meters into the near-wellbore region. Consequently, exploring the relationship of these near-well measurements with the properties more profound in the reservoir becomes a critical step in predicting the plume evolution with time. The observations obtained in this study indicate that the pH gradient analysis and the activity of aqueous species such as dissolved CO_2 and HCO_3^{-1} can provide trends that reflect the plume front evolution. In contrast, the depth profiles of CO_3^{-2} activity could not capture the plume behavior with time or depth.

4.3. On plume characteristics' sensitivity to well-based properties

In this study, we investigated the impact of various well-based properties on plume characteristics. This analysis is not a static process. De-

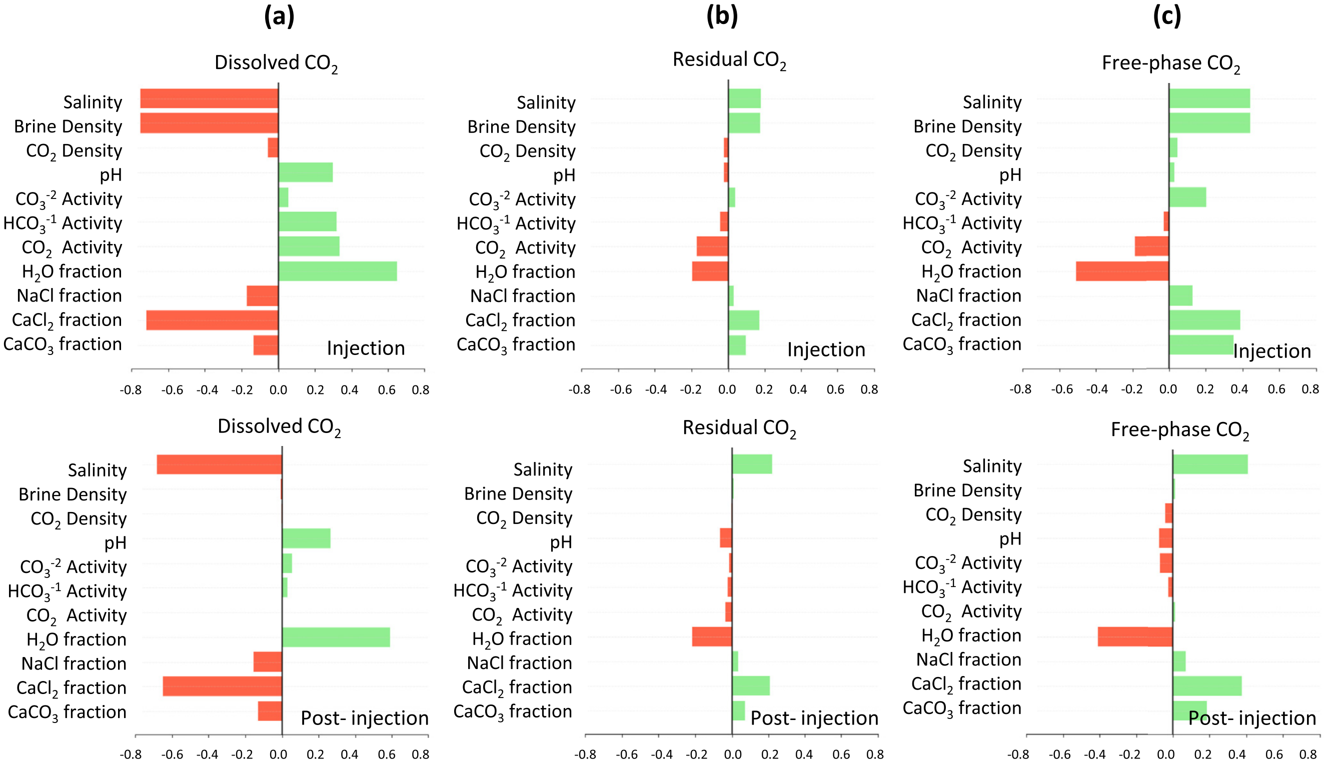

Fig. 14. The relative contribution of various fluid properties to the CO_2 distribution in the subsurface during injection and post-injection periods, including (a) dissolved CO_2 ratio, (b) residual CO_2 ratio, and (c) free-phase CO_2 ratio.

Table 5
Study's main questions and relevant findings.

	Question	Observations/Results
1	Which plume characteristics can we monitor using well-based variables?	The spatial characteristics of the CO_2 plumes included radial extent, vertical spread, and temporal evolution. The average radial extent of the plumes observed, as delineated by CO_2 dissolved in the aqueous phase, is typically more extensive than that for the plumes defined by supercritical CO_2. The average plume lateral growth has a linear relationship with the cumulative injected CO_2 in the log-log scale over a broad range. Also, the lateral expansion of the dissolved CO_2 plumes does not occur uniformly at various depths.
2	Can any well variables provide insights into the temporal evolution of the plumes?	Evaluation of the relationship between the evolution of selected fluid properties and the CO_2 plume dimensions suggests that not all the fluid properties exhibit a correlation. The pH changes can be more informative about the plume aspect ratio and radial extension, as well as the speciation and activities of CO_2 and HCO_3^{-1} in the aqueous phase. In contrast, the brine density and CO_3^{-2} activity do not significantly correlate with the plume dimensions, given that the original brine composition impacts them. As expected, operational variables such as the amount of CO_2 injected play a relevant role in the brine properties variation.
3	How representative are the near-wellbore fluid properties of the plume average properties?	The behavior of the parameters explored suggests that the pH gradient analysis and the activity of aqueous species such as dissolved CO_2 and HCO_3^{-1} can provide trends that reflect the plume region's evolution. In contrast, the depth profiles of CO_3^{-2} activity or the variations in brine density could not capture the plume behavior with time or depth.
4	How sensitive are the well variables to different plume dynamics metrics?	We explored the influence of various fluid properties on the plume dimensions, including salinity, pH, and carbonate speciation in the aqueous phase. The correlations observed suggest that fluid properties' relative influence on the plume dimensions changes during injection and post-injection periods. The plume radial extension depends on the CO_2 activity in the aqueous phase during the injection period, which correlates with the total CO_2 injected into the aquifer. For plume height, the salinity and brine density promote the plume height as they hinder the solubility of CO_2 into the aqueous phase.

pending on the scenarios investigated, the ranges used for the parameters and variables defining the aquifer system, and the physical processes considered, the different fluid properties' significance can differ. Moreover, the influence of the parameters investigated changes with time (during injection and post-injection periods), given that the injection of CO_2 influences the fluid properties behavior. We compiled the ranges from published and unpublished sources. For instance, the contents for temperature gradient are from Birkholzer et al. (2009), the molecular diffusion coefficients from Lu et al. (2013), and the saturation functions from Dana and Skoczylas (2002) and Krevor et al. (2012).

4.4. Limitations

The geochemical system employed is a simplified representation of the interactions at the aqueous phase, given that chemical systems in nature are overly complex. As a result, the fluid property variations and predictions become limited by an incomplete representation of the rock-fluid and fluid-fluid reactions. Including a more detailed mineral composition of the rocks and adding mineral-fluid interactions representing the immobilization of CO_2 can improve the model. Furthermore, considerations of physical and chemical processes at the pore scale become a requirement, including reactive transport and the effects of mechanical compaction on the pore structure. This reality implies the coupling of processes at different scales. Besides monitoring the plume evolution, surface and subsurface pressure and temperature monitoring will assist the injectivity question related to fault activation. For instance, the modified-Hall plot can reveal the formation parting or fault-activation pressure, as reported in a field setting in Norway (Aschehoug and Kabir, 2013), when excessive fluid injection occurs.

5. Conclusions

This study explored vital monitoring-related questions through a numerical investigation of carbon sequestration in saline aquifers during long-term and post-injection periods. The focus of the monitoring strategies was on the inference of the spatial and temporal characteristics of the CO_2 plumes in different forms: CO_2 dissolved in the aqueous phase, the pH change, supercritical CO_2, and the solid-phase saturation changes due to dissolution and precipitation, as discussed in Zapata et al. (2020). The monitorable properties considered included pH, brine density, and CO_2 speciation in the aqueous phase. We observed that the average radial extent of the plumes, delineated by CO_2 dissolved in the aqueous phase, is typically more extensive than that for the plumes defined by supercritical CO_2. The average plume lateral growth has a linear relationship with the cumulative injected CO_2 in the log-log scale over a broad range. Also, the lateral expansion of the dissolved CO_2 plumes does not occur uniformly at various depths. Below the injection point, dissolved CO_2 can extend laterally to a great length, driven by subsurface connectivity architecture and convective mixing.

Not all the fluid properties carry similar information content relevant to CO_2 sequestration well monitoring. Initial calcite presence in the aqueous phase determines the relationships between these variable pairs. The pH change can be more informative about CO_2 and $HCO_3{}^{-1}$ activities. The brine density does not exhibit a direct influence on the plume size. However, the distribution of CO_2 in distinct trapping mechanisms, such as solubility trapping, is correlated with the brine density, influencing the plume extension indirectly. In general, the near-well pH depth profiles can only capture the average plume profiles above the injection depth in most cases. Below the injection depth, this resemblance disappears in most cases.

During the injection period, the salinity and brine density promotes plume height as they hinder the solubility of CO_2 into the aqueous phase. The brine density and CO_2 speciation appear to have diminished the plume height growth in the post-injection period. However, brine salinity and density contribute to lateral plume growth. Once injection stopped, we observed a shift in the main parameters influencing the plume growth, with negligible influence from the CO_2 activity. This study did not explore items related to the wellbore's thermal integrity during CO_2 injection, salt precipitation or clogging, and wellbore leakage. Our future endeavors will attempt to address these practical issues by expanding the overall scope.

Declaration of Competing Interest

The authors declare that they have no known competing financial interests or personal relationships that could have appeared to influence the work reported in this paper

Acknowledgments

The authors thank Schlumberger and MathWorks for providing the software used in this study. This study received no funding.

Supplementary materials

Supplementary material associated with this article can be found, in the online version, at doi:10.1016/j.ccst.2022.100079.

References

Amin, M.S., Weiss, D.J., Blunt, M.J., 2014. Reactive transport modelling of geologic CO_2 sequestration in saline aquifers: The influence of pure CO_2 and of mixtures of CO_2 with CH_4 on the sealing capacity of cap rock at 37°C and 100 bar. Chem. Geol. 367, 39–50. doi:10.1016/j.chemgeo.2014.01.002.

Aschehoug, M., Kabir, C.S., 2013. Real-time evaluation of carbon dioxide production and sequestration in a gas field. SPE Res. Eval. Eng. 16 (2), 134–143.

Beaubien, S.E., Jones, D.G., Gal, F., Barkwith, A.K.A.P., Braibant, G., Baubron, J.C., Strutt, M.H., 2013. Monitoring of near-surface gas geochemistry at the Weyburn, Canada, CO_2-EOR site, 2001-2011. Int. J. Greenhouse Gas Control. 16 (1), S236–S262. doi:10.1016/j.ijggc.2013.01.013.

Beck, L., 2020. Carbon capture and storage in the USA: the role of US innovation leadership in climate-technnology commercialization. Clean Energy 4 (1), 2–11.

Benson, S.M., Cole, D.R., 2008. CO_2 sequestration in deep sedimentary formations. Elements 4 (5), 325–331. doi:10.2113/gselements.4.5.325.

Benson, S. M., Hoversten, M., Gasperikova, E., and Haines, M., 2005. Monitoring protocols and life-cycle costs for geologic storage of carbon dioxide, Greenhouse Gas Control Technologies 7, Proc. TTH Intl. Conf. Greenhouse Gas Control Technol. 5 Sept., vol. II - part 1, 1259–1264. https://doi.org/10.1016/B978-008044704-9/50136-1

Berntsen, A., Todorovic, J., Raphaug, M, Torsæter, M., Panduro, E.A.C., Gawel, K., 2019. Salt clogging during supercritical CO_2 injection into a downscaled borehole model. Int. J. Greenh. Gas Control 86, 201–210.

Birkholzer, J.T., Zhou, Q., Tsang, C., 2009. Large-scale impact of CO_2 storage in deep saline aquifers: a sensitivity study on pressure response in stratified systems. Greenh. Gas Control 3, 181–194.

Black, J.R., Carroll, S.A., Haese, R.R., 2015. Rates of mineral dissolution under CO_2 storage conditions. Chem. Geol. 399, 134–144. doi:10.1016/j.chemgeo.2014.09.020.

Bonto, M., Welch, M.J., Luthje, M., Nick, H.M., 2021. Challenges and enablers for large-scale CO_2 storage in chalk formations. Earth-Sci. Rev. 222, 103826.

Buckingham, J., Reina, T.R., Duyar, M.S., 2022. Recent advances in carbon dioxide capture for process intensification. Carbon Cap. Sci. Tech. 2, 100031.

Cao, C., Liao, J., Hou, Z., Wang, G., Feng, W., Fang, Y., 2020. Parametric uncertainty analysis for CO_2 sequestration based on distance correlation and support vector regression. J. Natural Gas Sci. Eng. 77 (May), 103237. doi:10.1016/j.jngse.2020.103237.

Chadwick, R.A., Arts, R., Bentham, M., Eiken, O., Holloway, S., Kirby, G.A., Zweigel, P., 2009. Review of monitoring issues and technologies associated with the long-term underground storage of carbon dioxide. Geological Soc. Special Pub 313, 257–275. doi:10.1144/SP313.15.

Dai, Z., Stauffer, P.H., Carey, J.W., Middleton, R.S., Lu, Z., Jacobs, J.F., Spangler, L.H., 2014. Pre-site characterization risk analysis for commercial-scale carbon sequestration. Environ. Sci. Technol. 48 (7), 3908–3915. doi:10.1021/es405468p.

Dana, E., Skoczylas, F., 2002. Experimental study of two-phase flow in three sandstones. II. Capillary pressure curve measurement and relative permeability pore space capillary models. Int. J. Multiph. Flow. 28 (12), 1965–1981. doi:10.1016/S0301-9322(02)00091-5.

De Silva, G.P.D., Ranjith, P.G., Perera, M.S.A., 2015. Geochemical aspects of CO_2 sequestration in deep saline aquifers: a review. Fuel 155, 128–143. doi:10.1016/j.fuel.2015.03.045.

Deng, H., Stauffer, P.H., Dai, Z., Jiao, Z., Surdam, R.C., 2012. Simulation of industrial-scale CO_2 storage: multi-scale heterogeneity and its impacts on storage capacity, injectivity, and leakage. Int. J. Greenh. Gas Control 10, 397–418. doi:10.1016/j.ijggc.2012.07.003.

Deutsch, C. V, and Journel, A. G. 1998. GSLIB Geostatistical software library and user's guide.

Duan, Z., Sun, R., 2003. An improved model calculating CO_2 solubility in pure water and aqueous NaCl solutions from 273 to 533 K and from 0 to 2000 bar.pdf. Chem. Geology 193, 257–271. doi:10.1016/s0009-2541(02)00263-2.

Emberley, S., Hutcheon, I., Shevalier, M., Durocher, K., Gunter, W.D., Perkins, E.H., 2004. Geochemical monitoring of fluid-rock interaction and CO_2 storage at the Weyburn CO_2-injection enhanced oil recovery site, Saskatchewan, Canada. Energy. 29 (9–10), 1393–1401. doi:10.1016/j.energy.2004.03.073.

Fenghour, A., Wakeham, W.A., Vesovic, V., 1998. The viscosity of carbon dioxide. J. Phys. Chem. Ref. Data. 27 (1), 31–44. doi:10.1063/1.556013.

Fessenden, J.E., Clegg, S.M., Rahn, T.A., Humphries, S.D., Baldridge, W.S., 2010. Novel MVA tools to track CO_2 seepage, tested at the ZERT controlled release site in Bozeman. MT. Environ. Earth Sci. 60 (2), 325–334. doi:10.1007/s12665-010-0489-3.

Freifeld, B.M., Daley, T.M., Hovorka, S.D., Henninges, J., Underschultz, J., Sharma, S., 2009. Recent advances in well-based monitoring of CO_2 sequestration. Energy Procedia 1 (1), 2277–2284. doi:10.1016/j.egypro.2009.01.296.

Freifeld, B.M., Trautz, R.C., Kharaka, Y.K., Phelps, T.J., Myer, L.R., Hovorka, S.D., Collins, D.J., 2005. The U-tube: a novel system for acquiring borehole fluid samples from a deep geologic CO_2 sequestration experiment. J. Geophys. Res. 110 (10), 1–10. doi:10.1029/2005JB003735.

Global CCS Institute, 2021. Global Status of CCS.

Gogri, M.P., Rohleder, J.M., Kabir, C.S., Pranter, M.J., Reza, Z.A, 2018. Prognosis for safe water-disposal-well operations and practices based on reservoir flow modeling and real-time performance analysis: SPE Res. Eval. Eng. 21 (3), 576–592. doi:10.2118/187083-PA.

Gholami, R., Raza, A., Iglauer, S., 2021. Leakage risk assessment of a CO_2 storage site: a review, 2021. Earth-Sci. Rev. 223, 103849.

Hannis, S.D., 2013. Monitoring the geological storage of CO_2. In: Geological Storage of Carbon Dioxide (CO_2): Geoscience, Technologies, Environmental Aspects and Legal Frameworks. Woodhead Publishing Limited, pp. 68–96. doi:10.1533/9780857097279.1.68.

Hassanzadeh, H., Pooladi-Darvish, M., Keith, D.W., 2005. Modelling of convective mixing in CO_2 storage. J. Can. Petrol. Tech. 44 (10), 43–51. doi:10.2118/05-10-04.

Hirschfelder, J.O., Bird, R.B., Spotz, E.L., 1949. The transport properties of gases and gaseous mixtures II. Chem. Rev. 44 (1), 205–231. doi:10.1021/cr60137a012.

Hovorka, S.D., Benson, S.M., Doughty, C., Freifeld, B.M., Sakurai, S., Daley, T.M., Knauss, K.G., 2006. Measuring permanence of CO_2 storage in saline formations: the Frio experiment. Environ. Geosci. 13 (2), 105–121. doi:10.1306/eg.11210505011.

Jiang, K., Ashworth, P., Zhang, S., Liang, X, Sun, Y., Angus, D., 2020. China's carbon capture, utilization and storage (CCUS) policy: a critical review. Renew. Sust. Energy Rev. 119, 109601.

Jayasekara, D.W., Ranjith, P.G., Wanniarachchi, W.A.M., Rathnaweera, T.D., 2020. Understanding the chemico-mineralogical changes of caprock sealing in deep saline CO_2 sequestration environments: a review study. J. Supercrit. Fluids. 161, 104819. doi:10.1016/j.supflu.2020.104819.

Jenkins, C., Chadwick, A., Hovorka, S.D., 2015. The state-of-the-art in monitoring and verification– ten years on. Int. J. Greenh. Gas Control. 40, 312–349. doi:10.1016/j.ijggc.2015.05.009.

Jones, D.G., Lister, T.R., Smith, D.J., West, J.M., Coombs, P., Gadalia, A., Lombardi, S., 2011. Salah gas CO_2 storage JIP: surface gas and biological monitoring. Energy Procedia 4, 3566–3573. doi:10.1016/j.egypro.2011.02.285.

Karstens, J., Ahmed, W., Berndt, C., Class, H., 2017. Focused fluid flow and the subseabed storage of CO_2: evaluating the leakage potential of seismic chimney structures for the Sleipner CO_2 storage operation. Marine Petrol. Geol. 88, 81–93. doi:10.1016/j.marpetgeo.2017.08.003.

Krevor, S.C.M., Pini, R., Zuo, L., Benson, S.M., 2012. Relative permeability and trapping of CO_2 and water in sandstone rocks at reservoir conditions. Water Res. Res. 48 (2), 1–16. doi:10.1029/2011WR010859.

Lagneau, V., Pipart, A., Catalette, H, 2005. Reactive transport modeling of CO_2 sequestration in deep saline aquifers. Oil Gas Sci. Technol. 60 (2), 231–247. doi:10.2516/ogst:2005014.

Lengler, U., De Lucia, M., Kühn, M., 2010. The impact of heterogeneity on the distribution of CO_2: numerical simulation of storage at Ketzin. Int. J. Greenh. Gas Control. 4 (6), 1016–1020. doi:10.1016/j.ijggc.2010.07.004.

Li, H., Lau, H.C., Wei, X., Liu, S., 2021. CO_2 storage potential in major oil and gas reservoirs in the northern south China sea. Int. J. Greenh. Gas Control. 108, 103328.

Lu, W., Guo, H., Chou, I.M., Burruss, R.C., Li, L., 2013. Determination of diffusion coefficients of carbon dioxide in water between 268 and 473 K in a high-pressure capillary optical cell with in situ Raman spectroscopic measurements. Geochim. Cosmochim. Acta 115, 183–204. doi:10.1016/j.gca.2013.04.010.

Martens, S., Conze, R., De Lucia, M., Henninges, J., Kempka, T., Liebscher, A., 2015. Joint research project CO_2MAN (CO_2MAN Reservoir Management): Continuation of reserach and development work for CO_2 storage at the Ketzin pilot site. In Geological Storage of CO_2 – Long Term Security Aspects (pp. 1–32).

Martin-Roberts, E., Scott, V., Flude, S., Gilfillan, S., 2021. Carbon capture and storage at the end of a lost decade. One Earth 4 (11), 1569–1584. doi:10.1016/j.oneear.2021.10.002.

McKay, M.D., Beckman, R.J., Conover, W.J., 2000. A comparison of three methods for selecting values of input variables in the analysis of output from a computer code. Technometrics 42 (1), 55–61. doi:10.2307/1271432.

Miri, R., Hellevang, H., 2016. Salt precipitation during CO_2 storage – a review. Int. J. Greenh. Gas Control 51, 136–147.

Nayak, N, Mehrotra, R., Mehrotra, S., 2022. Carbon biosequestration strategies: a review. Carbon Cap. Sci. & Tech. 4, 100065.

Norouzi, A.M., Babaei, M., Han, W.S., et al., 2021. CO_2-plume geothermal processes: a parametric study of salt precipitation influenced by capillary-driven backflow. Chem. Eng. J. 425, 130031.

Park, Y.C., Huh, D.G., Park, C.H., 2013. A sensitivity study of pressure monitoring to detect fluid leakage from geological CO_2 storage site. Energy Procedia 37, 4207–4214. doi:10.1016/j.egypro.2013.06.323.

Phan, T.N., Gogri, M.P., Kabir, C.S., Reza, Z., 2018. Exploring safe disposal of CO_2 and wastewater in saline aquifers. J. Petrol. Sci. Eng. 170, 197–205. doi:10.1016/j.petrol.2018.06.065.

Plackett, R.L., Burman, J.P., 1946. The design of optimum multifactorial experiments. Biometrika 33 (4), 305–325. doi:10.1093/biomet/33.4.305.

Plasynski, S.I., Litynski, J.T., McIlvried, H.G., Vikara, D.M., Srivastava, R.D., 2011. The critical role of monitoring, verification, and accounting for geologic carbon dioxide storage projects. Environ. Geosci. 18 (1), 19–34. doi:10.1306/eg.06231010008.

Rocha-Valadez, T., Hasan, A.R., Mannan, M.S., Kabir, C.S., 2014. Assessing wellbore integrity in sustained-casing-pressure annulus. SPE Drill. Compl. 29 (01), 131–138. doi:10.2118/169814-PA.

Roberts, J.J., Gilfillan, S.M.V., Stalker, L., Naylor, M., 2017. Geochemical tracers for monitoring offshore CO_2 stores. Int. J. Greenh. Gas Control. 65, 218–234. doi:10.1016/j.ijggc.2017.07.021.

Roy, P., Morris, J.P., Walsh, S.D.C., et al., 2018. Effect of thermal stress on wellbore integrity during CO_2 injection. Int. J. Greenh. Gas Control. 77, 14–20.

Sarkarfarshi, M., Malekzadeh, F., Gracie, R., Dusseault, M., 2014. Parametric sensitivity analysis for CO_2 geosequestration. Int. J. Greenh. Gas Control. 23, 61–71. doi:10.1016/j.ijggc.2014.02.003.

Savioli, G.B., Santos, J.E., Carcione, J.M., Gei, D., 2017. A model for CO_2 storage and seismic monitoring combining multiphase fluid flow and wave propagation simulators: the Sleipner-field case. Comput. Geosci. 21 (2), 223–239. doi:10.1007/s10596-016-9607-y.

Schlumberger, 2020. ECLIPSE, Industry-reference Reservoir Simulator. Technical Description, Houston, TX.

Shaw, R., Mukherjee, S., 2022. The development of carbon capture and storage (CCS) in India: a critical review. Carbon Capture Sci. Tech. 2, 100036.

Spycher, N., Pruess, K., 2005. CO_2-H_2O mixtures in the geological sequestration of CO_2, II, Partitioning in chloride brines at 12-100°C and up to 600 bar. Geochim. Cosmochim. Acta 69 (13), 3309–3320. doi:10.1016/j.gca.2005.01.015.

Spycher, N., Pruess, K., Ennis-King, J., 2003. CO_2-H_2O mixtures in the geological sequestration of CO_2, I, Assessment and calculation of mutual solubilities from 12 to 100°C and up to 600 bar. Geochim. Cosmochim. Acta 67 (16), 3015–3031. doi:10.1016/S0016-7037(03)00273-4.

Steefel, C. I. 2008. Geochemical kinetics and transport. In Kinetics of Water-Rock Interaction (pp. 545–589). https://doi.org/10.1007/978-0-387-73563-4_11

Sun, A.Y., Lu, J., Freifeld, B.M., Hovorka, S.D., Islam, A., 2016. Using pulse testing for leakage detection in carbon storage reservoirs: A field demonstration. Int. J. Greenh. Gas Control. 46, 215–227. doi:10.1016/j.ijggc.2016.01.015.

Trainor-Guitton, W., Mansoor, K., Sun, Y., Carroll, S, 2016. Merits of pressure and geochemical data as indicators of CO_2/brine leakage into a heterogeneous, sedimentary aquifer. Int. J. Greenh. Gas Control. 52, 237–249. doi:10.1016/j.ijggc.2016.07.002.

Vesovic, V., Wakeham, W.A., Olchowy, G.A., Sengers, J.V., Watson, J.T.R., Millat, J., 1990. The transport properties of carbon dioxide. J. Phys. Chem. Ref. Data 19 (3), 763–808. doi:10.1063/1.555875.

Vo Thanh, H., Sugai, Y., Nguele, R., Sasaki, K., 2019. Integrated workflow in 3D geological model construction for evaluation of CO_2 storage capacity of a fractured basement reservoir in Cuu Long Basin, Vietnam. Int. J. Greenh. Gas Control. 90 (August), 102826. doi:10.1016/j.ijggc.2019.102826.

Würdemann, H., Möller, F., Kühn, M., Heidug, W., Christensen, N.P., Borm, G., Schilling, F.R., 2010. CO_2SINK-From site characterisation and risk assessment to monitoring and verification: one year of operational experience with the field laboratory for CO_2 storage at Ketzin, Germany. Int. J. Greenh. Gas Control. 4 (6), 938–951. doi:10.1016/j.ijggc.2010.08.010.

Xu, T., Apps, J.A., Pruess, K., 2004. Numerical simulation of CO_2 disposal by mineral trapping in deep aquifers. Appl. Geochem. 19 (6), 917–936. doi:10.1016/j.apgeochem.2003.11.003.

Xue, Z., Tanase, D., Watanabe, J., 2006. Estimation of CO_2 saturation from time-lapse CO_2 well logging in an Onshore Aquifer, Nagaoka, Japan. Explor. Geophys. 37 (1), 19–29. doi:10.1071/EG06019.

Zapata, Y., 2020. Multiscale, Multiphysics Modeling of Subsurface Engineering Applications. Doctoral Dissertation, University of Oklahoma.

Zapata, Y., Kristensen, M.R., Huerta, N., Brown, C., Kabir, C.S., Reza, Z., 2020. CO_2 geological storage: Critical insights on plume dynamics and storage efficiency during long-term injection and post-injection periods. J. Natural Gas Sci. Eng. 83 (July), 103542. doi:10.1016/j.jngse.2020.103542.

Zaytsev, I.D., Aseyev, G.G., 1992. Properties of Aqueous Solutions of Electrolytes. CRC Press, Boca Raton, Florida LC: 92025367.